


Sound source characteristics generated by shocklets in isotropic compressible turbulence

Daiki Terakado ^{*}

Department of Aeronautics and Astronautics, The University of Tokyo, Tokyo 1138656 Japan

Taku Nonomura  and Soshi Kawai 

Department of Aerospace Engineering, Tohoku University, Sendai 9808579, Japan

Hikaru Aono 

Department of Mechanical Engineering and Robotics, Shinshu University, Ueda 3868567, Japan

Makoto Sato 

Department of Mechanical Science and Engineering, Kougakuin University, Tokyo 1638677, Japan

Akira Oyama 

Institute of Space and Astronautical Science, JAXA, Sagami-hara 2525210, Japan

Kozo Fujii 

*Institute of Space and Astronautical Science, JAXA, Sagami-hara 2525210, Japan
and Department of Information and Computer Technology, Tokyo University of Science,
Tokyo 1258585, Japan*



(Received 11 April 2021; accepted 10 May 2022; published 19 August 2022;
corrected 6 September 2022)

This study analyzes the effects of shocklets on sound source characteristics using direct numerical simulations. The sound sources are obtained from the source terms of the Lighthill equation. The highest initial turbulent Mach number M_{t0} is set to be 1.0, and the strong effects of shocklets on sound sources are investigated. Results show that the occurrence of shocklets in high turbulent Mach numbers $M_{t0} \geq 0.7$ affects the sound generation mechanism in addition to vortical motions which are well-known sound sources in low Mach number turbulent flows. The change in mechanism influences the relationship between the Reynolds stress and entropy terms. For low turbulent Mach number flows without shocklets, the Reynolds stress and entropy terms partially show the same signs around and on vortices. However, for high turbulent Mach numbers with shocklets, the terms exhibit opposite signs across shocklets. The behaviors of the Reynolds stress and entropy terms across shocklets are explained analytically by using a one-dimensional shock relation. The change in sound source characteristics keeps velocity dependence on total sound source strength almost unchanged independent of the turbulent Mach number, though each term's sound source strength (normalized by the total sound source strength) becomes larger for the higher turbulent Mach numbers $M_{t0} \geq 0.9$ than those for low turbulent Mach numbers $M_{t0} \leq 0.4$. Besides, the applicability of the present study to predict far-field acoustic wave characteristics is discussed. The source terms based on

^{*}Currently at Research and Development Directorate, Japan Aerospace Exploration Agency, Tsukuba, 3058505 Japan; terakado.daiki@jaxa.jp

Lilley's decomposition show that the sound sources derived by shocklets have quadruple characteristics. Also, it is shown that the given knowledge in the present study, especially for the relation between the Reynolds stress and entropy terms across shocklets, can be used to improve the source modeling for a nonlinear acoustic analogy based on the Lighthill's acoustic analogy and Burgers' equation. In addition, the paper provides a possible explanation of the contributions of the shocklets for a mechanism of crackle noise that the generated acoustic waves by shocklets propagates to the acoustic field and show high-frequency spectral characteristics.

DOI: [10.1103/PhysRevFluids.7.084605](https://doi.org/10.1103/PhysRevFluids.7.084605)

I. INTRODUCTION

Isotropic turbulence is one of the most important flows to understand the fundamental knowledge not only for turbulent flows but also for aeroacoustic problems.

With the framework of Lighthill's acoustic analogy [1], Proudman [2] first showed that the acoustic power in the far field is proportional to the fifth power of the turbulent Mach number $M_t = \langle u_i^2 \rangle^{1/2} / \langle c \rangle$ defined with root mean square of the velocity fluctuation and the speed of sound. Lilley [3] developed the theory considering with the retarded time later. The validity of the theories was examined with direct numerical simulations (DNS) [4,5] and large-eddy simulations (LES) [5]. In addition, Lilley [6] extended the theory to the hot fluid flow and applied the developed theory to the prediction of subsonic to supersonic fully expanded hot jet flows. The results showed that the predicted acoustic wave characteristics by the developed theory were in good agreement with those of experimental data. Because of the simplicity and availability of the theory validated with the high-fidelity simulations of DNS and LES, isotropic turbulence has been used as a benchmark problem for the prediction method of the acoustic waves from turbulent fluid flows as well. A hybrid approach with LES is one of the most powerful tools for aeroacoustic problems today in which unsteady turbulent flow is computed with LES and far-field acoustic waves are predicted with the acoustic analogy. In the method, however, there is a so-called missing noise problem where the acoustic waves generated from the subgrid scale (SGS) cannot be reproduced unless given appropriate modeling. Isotropic turbulence has been used for the investigation of the modeling. Seror *et al.* [7,8] showed that the consideration of the subgrid-scale tensor of the Lighthill equation is required to reproduce the acoustic field given by DNS. They used a scale-similarity-type SGS model and recovered the acoustic field. For the eddy-viscosity-type SGS models, He *et al.* [9] reported that the dynamic Smagorinsky model was the best in the range they investigated. There is a study from a theoretical approach as well. Rubinstein and Zhou [10] revealed that high-frequency acoustic waves are governed by the Eulerian space-time correlation rather than the Lagrangian counterpart, and it leads to different scaling of the acoustic wave spectra in a high-frequency range. Their study was confirmed by DNS [9] later.

Thus far, isotropic turbulence has contributed to the comprehension of the fundamental knowledge of the acoustic waves generated by turbulence and has offered an effective *a priori* testbed. However, the previous studies were limited to the low turbulent Mach number range regardless of its importance for the high turbulent Mach number flows. For example, one possible explanation for crackle noise would be generated by high fluctuating turbulent flow or high turbulent Mach number flow. The crackle noise generated by high-thrust military aircraft jets shows shocklike N-shaped acoustic waves with sharp compression and high skewness of pressure $S_k(p') > 0.4$ [11]. Two possible explanations are believed to exist for the generated high skewed pressure waves. One is the nonlinear propagation effects [12–15]. The other is that the skewed pressure waves are originated from turbulent fluctuation as the sound source [16–20]. For the latter, though recent papers [19,20] showed that the high skewed pressure was caused by steepened Mach waves generated by the large-scale turbulent structure of turbulence, there still exist unrevealed points. In their studies, the

spectral characteristics in crackle generating conditions have not been discussed in detail. In fact, the conditional averaged flow given in the study by Pineau and Bogey [20] does not reproduce the high wave number spectral characteristics, which would be related to fine-scale turbulence. One of our motivations for the present study is to understand the contributions of fine-scale turbulence to the mechanism of crackle noise.

Moderate-to-high turbulent Mach number flows, $M_t \geq 0.4$ for the representative case, generating locally supersonic velocity fluctuations to lead occurrence of shocklets show significantly different characteristics compared with that of low turbulent Mach numbers. The existence of shocklets was first reported by Passot and Pouquet [21] in two dimensions and by Lee *et al.* [22] in three dimensions. Although shocklet volume is only a few percent of the total volume of the computational region, shocklets strongly affect the turbulence properties [23,24]. Lee *et al.* [22] conducted DNS of the isotropic decaying compressible turbulence and confirmed that shocklets and shock waves exhibit the same properties. They demonstrated that the compressible dissipation around shocklets is ten times larger than the typical incompressible turbulence because the pressure is highly correlated with dilatation in shocklet regions, and the kinetic energy converts to internal energy. Shocklets significantly affect the dynamics of the vortices; the overall enstrophy production is remarkably suppressed when the Mach number is sufficiently high $M_{t0} \geq 0.4$ for the shocklets to appear [24]. Note that, locally, shocklets intensify enstrophy production in the shocklets region [25,26]. Also, shocklets can elongate the tail of the teardrop-shaped joint probability density function of the second and third invariants of the velocity gradient tensor compared to incompressible turbulence [24,27]. These previous studies clearly demonstrate that the occurrence of shocklets considerably changes flow fields in moderate-to-high turbulent Mach numbers.

In the present study, we investigate the effects of the occurrence of shocklets on the sound generation mechanism in moderate-to-high turbulent Mach number flows with isotropic compressible turbulence using DNS. The source terms of the Lighthill equation are directly computed from the given flow field by DNS and analyzed. A similar analysis was conducted by Choi *et al.* [28] for temporally evolving turbulent flow, but for low convective Mach number flow (leading to low turbulent Mach number flow). In order to help to understand the sound source characteristics of high turbulent Mach number flow, the low turbulent Mach number flow is also analyzed for comparison. The Lighthill equation is selected for analyzing sound source characteristics in the present study, because it is the most fundamental equation of aeroacoustics today, and thus should be good as a starting point both for understanding the sound generation mechanism and for future sound source modeling. It is worth noting that Miller [29] proposed a nonlinear acoustic analogy by the combination of the sound source spectra given by Lighthill's acoustic analogy and Burgers' equation, and showed that the possibility to predict the acoustic waves generated by the high Mach number and/or heated jets. Thus, the results given in the present paper will be utilized for the improvement of the source model, we believe. The applicability of the present analysis is discussed in Sec. III E.

The remainder of this paper is organized as follows. Section II presents the numerical method adopted herein. Section III describes the results obtained. Section III A discusses the grid and domain sensitivity for verifying the computational results, and the turbulent Mach number dependence is investigated in Sec. III B. The detailed characteristics for low and high turbulent Mach number cases are shown and the underlying mechanism is discussed in Secs. III C and III D. Section III E summarizes the applicability of the present analysis and shows a possible explanation for the mechanism of crackle as an important application of the current results. Finally, Sec. IV concludes the study.

II. PROBLEM SETUP AND METHODS

Decaying compressible turbulence is simulated in a cubic box of size 2π with periodic boundary conditions. The governing equations are three-dimensional compressible Navier-Stokes equations in

nondimensional form for an ideal gas:

$$\frac{\partial \rho}{\partial t} + \frac{\partial(\rho u_j)}{\partial x_j} = 0, \quad (1)$$

$$\frac{\partial(\rho u_i)}{\partial t} + \frac{\partial(\rho u_i u_j + p \delta_{ij})}{\partial x_j} = \frac{M}{\text{Re}} \frac{\partial \sigma_{ij}}{\partial x_j}, \quad (2)$$

$$\frac{\partial e}{\partial t} + \frac{\partial((e+p)u_j)}{\partial x_j} = \frac{M}{\text{Re}} \left(\frac{\partial(u_i \sigma_{ij})}{\partial x_j} - \frac{\partial q_j}{\partial x_j} \right), \quad (3)$$

where e is the total energy per unit volume. The viscous stress tensor σ_{ij} and the heat flux vector q_i are defined as

$$\begin{aligned} \sigma_{ij} &= \mu \left(\frac{\partial u_i}{\partial x_j} + \frac{\partial u_j}{\partial x_i} - \frac{2}{3} \frac{\partial u_k}{\partial x_k} \right), \\ q_i &= -\kappa \frac{\partial T}{\partial x_i} \\ &= -\frac{\mu}{\text{Pr}(\gamma - 1)} \frac{\partial c^2}{\partial x_i}. \end{aligned}$$

The equations are nondimensionalized with the reference length L_{ref}^* , speed of sound c_{ref}^* , density ρ_{ref}^* , and viscosity μ_{ref}^* . $\text{Re} = \rho_{\text{ref}}^* U_{\text{ref}}^* L_{\text{ref}}^* / \mu_{\text{ref}}^*$ is the reference Reynolds number, and $M = U_{\text{ref}}^* / c_{\text{ref}}^*$ is the reference Mach number. In the present simulations, the viscosity, μ , is determined using Sutherland's law, and the specific heat ratio, γ , and the Prandtl number, $\text{Pr} = c_p^* \mu^* / \kappa^*$, are kept constant at 1.4 and 0.72, respectively, where c_p^* is the specific heat at constant pressure and κ is the thermal conductivity.

The equations are solved using the hybrid approach capturing shocklets and resolving turbulence with high accuracy. The sixth-order, skew-symmetric splitting scheme [30] is adopted for smooth regions. For shock capturing, the dissipation term [31] of the sixth-order weighted, essentially nonoscillatory central upwind scheme [32] is added to shock regions that are identified by the Ducros sensor [33]. The time advancement is performed using the fourth-order Runge-Kutta scheme.

In the simulation of the isotropic compressible turbulence, there are choices between decaying and forced turbulence. Both simulated flows show some dependence on their numerical setup. The characteristics of simulated flow depend on the initial condition for decaying compressible turbulence [23–25,34–37], while they depend on the way of forcing [38–40] for forced compressible turbulence simulation. Then, in the present simulation, as a first step, we choose the simplest flow configuration of the decaying isotropic compressible turbulence. Although the better discussion could be done using a time-averaged characteristic with forced turbulence, our decaying turbulence simulation reaches a quasi-steady state, and therefore, eliminates the effects of transient as discussed in Sec. III A. Thus, the simulated flow characteristics should be related to the time-averaged characteristics obtained by the forced turbulence. With regard to the initial condition, an initially solenoidal and isentropic fluctuation [37] is employed and the artificial entropy fluctuation that generates a sound source term in the Lighthill equation [1] is carefully eliminated. The sound source term is negligible in low Mach number turbulent flows. The effects of the initial entropy distributions on the flow were reported by Terakado and Hattori [37]. They demonstrated that the initially uniform entropy condition stays uniform, supporting the fact that the present initial condition substantially suppresses the artificial entropy fluctuation. Initially, solenoidal velocity is also discussed herein. The initial ratio of the compressive component to the incompressible component of the velocity can influence the critical turbulent Mach number for generating shocklets as well as the shocklet strength [24,25,37]. However, the basic characteristics of shocklets remain unchanged. This implies that the effect of shocklets on sound sources which is one of the main topics of the present paper can be discussed regardless of the initial solenoidality. Then, for simplicity, we choose the initial

solenoidal velocity with various turbulent Mach numbers that are most used in the previous isotropic compressible decaying turbulence simulations [23,24,41].

The brief procedure for generating the initial condition is described below. The velocity distribution is determined by giving the spectrum of a final state of decaying turbulence:

$$E(k) \sim k^4 \exp\left(-2\frac{k^2}{k_{\text{peak}}^2}\right), \quad (4)$$

where k represents the magnitude of the wave number in space and $k_{\text{peak}} = \sqrt{10}$ is the peak wave number of the spectrum. The amplitudes and phases are randomized by a random seed. The solenoidal condition is satisfied by subtracting the compressive component $\hat{\mathbf{u}}_c$ from velocity fields. The compressive component $\hat{\mathbf{u}}_c$ is written as

$$\hat{\mathbf{u}}_c = \frac{\mathbf{k} \cdot \mathbf{u}}{|\mathbf{k}|} \mathbf{k}, \quad (5)$$

where \mathbf{u} is the velocity vector and \mathbf{k} is the wave number vector. The amplitudes of the given velocity field are adjusted depending on the initial turbulent Mach numbers. The pressure and density (p and ρ) are determined by a Poisson equation derived from the momentum equation in the inviscid flow [37]:

$$\nabla^2\left(\frac{p}{\rho}\right) = -\frac{\gamma-1}{\gamma} \frac{\partial^2(u_i u_j)}{\partial x_i \partial x_j}. \quad (6)$$

The equation is solved with the isentropic relation $p/\rho^\gamma = p_\infty/\rho_\infty^\gamma$, where p_∞ and ρ_∞ are the reference values of pressure and density in the nondimensional equations, respectively. In the present simulation, the initial turbulent Mach number, $M_t = \langle u_i^2 \rangle^{1/2}/c$, and the Taylor microscale Reynolds number, $R_\lambda = \langle u_i^2/3 \rangle^{1/2} \lambda \langle \rho \rangle / \langle \mu \rangle$, are set to be $M_{t0} = 0.1-1.0$ and $R_\lambda = 70-130$, respectively. The Taylor microscale λ is defined to be $\lambda = \sqrt{\langle u_i^2/3 \rangle / \langle (\partial u_i / \partial x_i)^2/3 \rangle}$, where $\langle \rangle$ denotes a spatially averaged quantity.

III. RESULTS AND DISCUSSION

Simulation parameters are shown in Table I. A total of 15 cases are computed. The main discussion is conducted for the highest Reynolds number, $R_{\lambda 0} = 130$, corresponding to series A, whereas the lower Reynolds numbers, $R_{\lambda 0} = 100$ and $R_{\lambda 0} = 70$ (series B and C), are employed for the investigation of the Reynolds number dependence. A10' and A10'' are used for a verification study. The normalization is conducted by the root mean square (rms) of the considered values unless otherwise noted.

A. Quasi-steady state and grid sensitivity

The isotropic compressible turbulence decays temporally; therefore, the time required for comparison between computed cases must be determined. Herein, the time is normalized using the initial values of the large eddy turnover time, $\tau = L_I / \sqrt{\langle u_i^2/3 \rangle}$. The integral scale, L_I , is defined as

$$L_I = \frac{3\pi}{2\sqrt{\langle u_i^2 \rangle}} \int_0^{k_{\text{max}}} \frac{E(k)}{k} dk, \quad (7)$$

where k is the magnitude of the wave number. For determining a quasi-steady state, the enstrophy, $W = \langle |\omega|^2 \rangle$, and the velocity derivative skewness, S_k , are often used in decaying isotropic turbulence, where ω is vorticity [42,43]. The velocity derivative skewness is defined as follows:

$$S_k = \frac{\langle ((\partial u_i / \partial x_i)^3 / 3) \rangle}{\langle ((\partial u_i / \partial x_i)^2 / 3) \rangle^{3/2}}. \quad (8)$$

TABLE I. Parameters used in the present direct numerical simulations. N^3 is the resolution. M_{t0} and $R_{\lambda0}$ are the initial values of the turbulent Mach number and the Taylor microscale Reynolds number. $M_{t\text{ st}}$, $R_{\lambda\text{ st}}$, and $k_{\text{max}}\eta$ are the respective turbulent Mach number, Taylor microscale Reynolds number, and the resolution parameter at the steady state: $t/\tau_0 = 3$ for case A, $t/\tau_0 = 2.78$ for case B, and $t/\tau_0 = 2.39$ for case C, where τ_0 is the initial value of the large eddy turnover time.

Case	N^3	M_{t0}	$R_{\lambda0}$	$M_{t\text{ st}}$	$R_{\lambda\text{ st}}$	$k_{\text{max}}\eta$
A02	512^3	0.2	130	0.11	32	6.29
A03	512^3	0.3	130	0.17	32	6.31
A04	512^3	0.4	130	0.22	32	6.35
A05	512^3	0.5	130	0.29	33	6.40
A06	512^3	0.6	130	0.33	33	6.49
A07	512^3	0.7	130	0.38	33	6.59
A08	512^3	0.8	130	0.42	33	6.75
A09	512^3	0.9	130	0.45	33	6.91
A10	512^3	1.0	130	0.48	32	7.22
A10'	384^3	1.0	130	0.48	22	5.34
A10''	256^3	1.0	130	0.46	24	3.69
B02	384^3	0.2	100	0.12	29	5.59
B10	384^3	1.0	100	0.48	28	6.44
C02	256^3	0.2	70	0.12	24	4.96
C10	256^3	1.0	70	0.48	24	5.64

The time history of the enstrophy and the velocity derivative skewness for $R_{\lambda0} = 130$ are shown in Figs. 1(a) and 1(b), respectively. The enstrophy is normalized by its initial value. The enstrophy passes the peak after $t/\tau_0 \simeq 2$ and the velocity derivative skewness reaches a steady negative value of approximately -0.5 at $t/\tau_0 \simeq 3$ for all the cases. This indicates that turbulence sufficiently develops and shows nonlinear dynamics with the smallest scales. Therefore, the time, $t/\tau_0 = 3$, is determined to be in a steady state and the results are compared at that time. At $t/\tau_0 = 3$, the kinetic energy, $E = \langle u_i^2 \rangle$, decreases to approximately one-third of the initial state for all the cases and decays in almost the same way for all cases except for the initial transient in Fig. 2. The low Reynolds number cases develop faster than the cases of $R_{\lambda0} = 130$; for a fair comparison, the times $t/\tau_0 = 2.39$ and $t/\tau_0 = 2.78$ are selected for $R_{\lambda0} = 70$ and $R_{\lambda0} = 100$, respectively, when

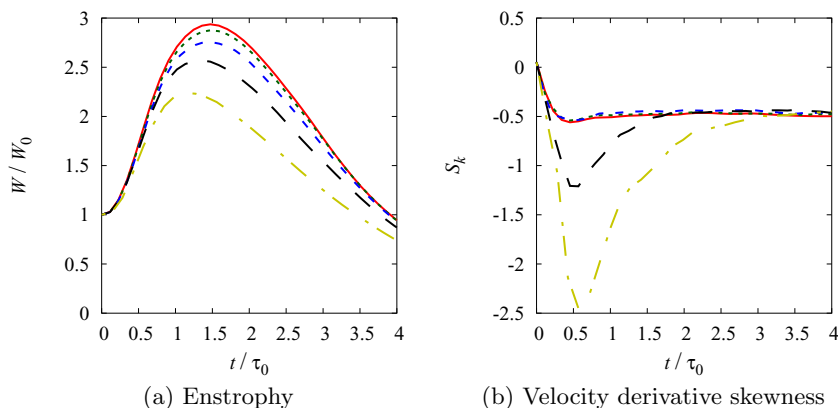


FIG. 1. Time history of (a) enstrophy, (b) velocity derivative skewness for $R_{\lambda0} = 130$: — (red), $M_{t0} = 0.2$; \cdots (green), $M_{t0} = 0.4$; - - (blue), $M_{t0} = 0.6$; - · - (black), $M_{t0} = 0.8$; - · - (yellow), $M_{t0} = 1.0$. Note that the value of enstrophy is normalized by its initial value.

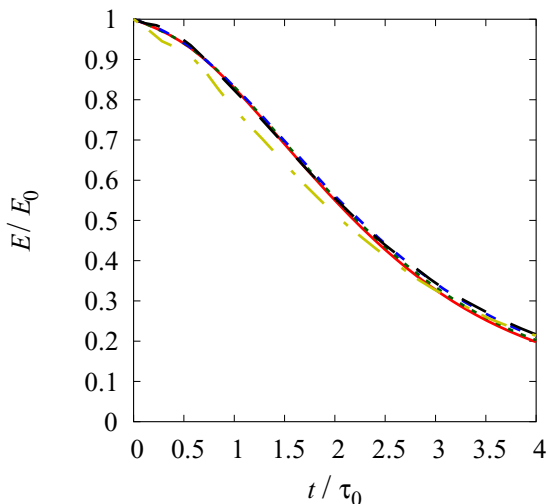


FIG. 2. Time history of kinetic energy for $R_{\lambda 0} = 130$: — (red), $M_{t0} = 0.2$; \cdots (green), $M_{t0} = 0.4$; - - (blue), $M_{t0} = 0.6$; - - - (black), $M_{t0} = 0.8$; - · - (yellow), $M_{t0} = 1.0$. The value for kinetic energy is normalized by its initial value.

the kinetic energy reaches one-third of each initial value. At the selected times, the enstrophy and the velocity derivative skewness also show the similar nonlinear characteristics discussed above. The selected times are used in the following discussion.

The velocity power spectra with different grid resolutions are evaluated and the grid sensitivity is assessed. Here two components of the velocity are considered based on the Helmholtz decomposition,

$$\mathbf{u} = \mathbf{u}^i + \mathbf{u}^c, \quad (9)$$

where the incompressible component, \mathbf{u}^i , and the compressive component, \mathbf{u}^c , satisfy $\nabla \cdot \mathbf{u}^i = 0$ and $\nabla \times \mathbf{u}^c = \mathbf{0}$, respectively. The case $M_{t0} = 1.0$ with $R_{\lambda 0} = 130$ is shown in Fig. 3 with different grid resolutions, where the selected case shows the highest probability of shocklet occurrence

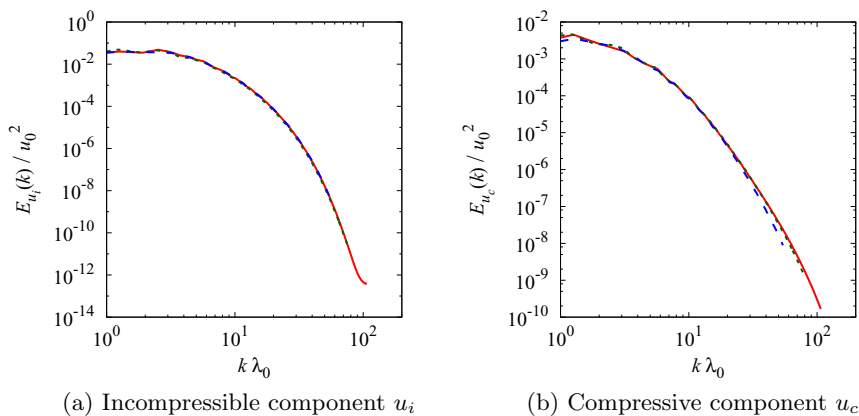


FIG. 3. Velocity spectra of two components, (a) incompressible component and (b) compressive component for $M_{t0} = 1.0$, $R_{\lambda 0} = 130$ at $t/\tau_0 = 3$: — (red), $N^3 = 512^3$; \cdots (green), $N^3 = 384^3$; - - (blue), $N^3 = 256^3$.

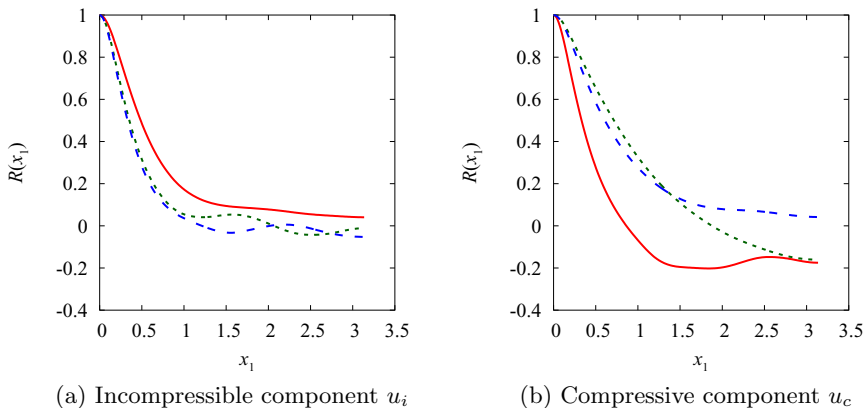


FIG. 4. Autocorrelations of the (a) incompressible velocity u_i and (b) compressive velocity u_c for $M_{t0} = 1.0$, $R_{\lambda 0} = 130$ at $t/\tau_0 = 3$: — (red), x_1 component; \cdots (green), x_2 component; - - (blue), x_3 component.

such that the required resolution is the highest. In all the cases, the spectra of the incompressible component demonstrate consistent agreement. The grid resolution, $N^3 = 512$, achieves sufficient grid convergence for the compressive component of the velocity spectra, which are closely related to shocklets. The resolution parameter, $k_{\max}\eta$, based on the maximum value of the wave number, k_{\max} , and the Kolmogorov length scale, $\eta = [(\mu/\rho)^3/(\varepsilon/\rho)]^{1/4}$, is also shown in Table I. Note that $\varepsilon = \sigma_{ij}\partial u_i/\partial x_j$ is the dissipation. All the cases except for the verification case A10'' show $k_{\max}\eta \simeq 5$ or larger, which are much larger values than the criteria for a DNS of incompressible turbulence $k_{\max} \simeq 1$. Hence, the smallest scale turbulent characteristics are well resolved in the present simulations. The higher grid resolutions than the criteria of incompressible DNS are employed, and the characteristics of shocklets, which impact sound sources in high turbulent Mach numbers, are captured well. Overall, the smallest scale of turbulence is well resolved and shocklets are well captured in the present simulations. The same confirmation has been conducted also for $R_{\lambda 0} = 100$ and $R_{\lambda 0} = 70$, and the grid resolutions $N^3 = 384^3$ and $N^3 = 256^3$ are selected for those cases, respectively.

The effects of periodicity should be discussed for isotropic turbulence. Ishida *et al.* [44] explained, in their DNS of incompressible isotropic turbulence, that the spurious effects on correlation caused by periodicity can be ignored when the domain size l_{box} satisfies $l_{\text{box}}/l \geq 2\pi \times 20 \sim 126$, where $l = 1/k_{\text{peak}}$ is an integral scale based on the peak wave number of the initial energy spectra. The present simulation result, $l_{\text{box}}/l = 2\pi \times \sqrt{10} \sim 20$, does not satisfy the required criteria; therefore, the effects of periodicity on correlation must be checked. Figure 4 shows the autocorrelations of incompressible and compressive velocities for the x_1 direction. The correlation of incompressible component reaches almost zero with increasing distance; thus, the effects of periodicity on incompressible component can almost be ignored. In contrast, the correlation of a compressive component has a large value due to a longer wave number compared to that of incompressible component. However, its absolute value is < 0.2 at the farthest point inside the computational box. Further, the main characteristics of sound sources do not change depending on the Reynolds number (see Secs. III C and III D), which implies that the main characteristics of the sound sources do not depend on the ratio of the domain size and the length scale of turbulence. These facts support that the present domain size is acceptable for the main discussion of sound source characteristics. It should also be noted that the relationship between shocklets and sound source characteristics, which is the main finding in the present paper, is clearly explained by the 1D shock relation as shown in Sec. III D. Thus, the domain size does not affect the conclusion presented in this paper.

B. Mach number dependence on sound sources

In this subsection, the overall trend of the turbulent Mach number dependence on the source terms of the Lighthill equation is analyzed for the cases wherein $R_{\lambda 0} = 130$. The Lighthill equation [1] in the nondimensional form is described as follows:

$$\frac{\partial^2 \rho}{\partial t^2} - \nabla^2 \rho = \frac{\partial^2 T_{ij}}{\partial x_i \partial x_j}, \quad (10)$$

where T_{ij} is Lighthill's turbulent stress tensor written as

$$T_{ij} = \rho u_i u_j + \delta_{ij}(p - \rho) + \frac{M}{\text{Re}} \sigma_{ij}. \quad (11)$$

Herein, these values are set as spatially averaged values of the initial conditions. Since the nondimensionalization is conducted with the speed of sound, it does not appear in the nondimensional Lighthill equation above. The second term of the entropy component is zero when the flow is isentropic; hence, it is often neglected in low Mach number flows. The third term is the viscous stress tensor σ_{ij} . For high Reynolds number conditions, the third term is also considered negligible. Thus, the first term of the Reynolds stress contribution is often considered to be the main sound source in low Mach number turbulent flows. All these components are analyzed because the characteristics of three terms in the high turbulent Mach number cases have not been discussed well. A previous study showed that the entropy term has a nonnegligible value even in the low convective Mach number mixing layer due to the dissipation generated around vortices [28]; thus, all components should be carefully discussed in the entire range of the turbulent Mach numbers that are investigated herein. The sound source characteristics are investigated herein not by Lighthill's turbulent stress tensor T_{ij} but by the source term $\partial^2 T_{ij} / \partial x_i \partial x_j$. The sound sources are decomposed into the following three terms:

$$\begin{aligned} S_{\text{Re}} &= \frac{\partial^2 (\rho u_i u_j)}{\partial x_i \partial x_j}, \\ S_{\text{en}} &= \frac{\partial^2 (\delta_{ij}(p - \rho))}{\partial x_i \partial x_j}, \\ S_{\text{vis}} &= \frac{\partial^2 \left(\frac{M}{\text{Re}} \sigma_{ij} \right)}{\partial x_i \partial x_j}, \\ S_{\text{all}} &= S_{\text{Re}} + S_{\text{en}} + S_{\text{vis}}, \end{aligned} \quad (12)$$

where S_{Re} , S_{en} , S_{vis} , and S_{all} are the Reynolds stress term, entropy term, viscous term and sum of all the terms (term total), respectively. First, the contributions of each source term are analyzed. The sound source strength is defined by the square of the source term. The ratio of each source term to the term total in the sound source strength is shown in Fig. 5. The quantities discussed herein are spatially averaged. The Reynolds stress term has the largest contribution over the range of the turbulent Mach numbers, as expected. However, the entropy term is not negligible, with values of ~ 0.25 even for the low turbulent Mach number cases, which differs from the theoretical prediction. The viscous term is not negligible for the high turbulent Mach number cases ($M_{t0} \geq 0.8$). For $M_{t0} = 1.0$, the viscous term is ~ 0.1 . Notably, the ratio of the Reynolds stress term exceeds the value of unity for $M_{t0} = 1.0$; thus, two or all terms show more or less opposite signs. In contrast, for the low turbulent Mach number cases, some source terms show the same signs because each value is below unity. Next, the relation between the terms is discussed in detail, examining the spectral characteristics and velocity dependence.

For the spectra, the normalization is conducted by the initial values of the density ρ_0 , the magnitude of velocity u_0 , and the Taylor microscale λ_0 , where each value is spatially averaged. Figure 6 displays sound source spectra for the five different turbulent Mach number cases. The

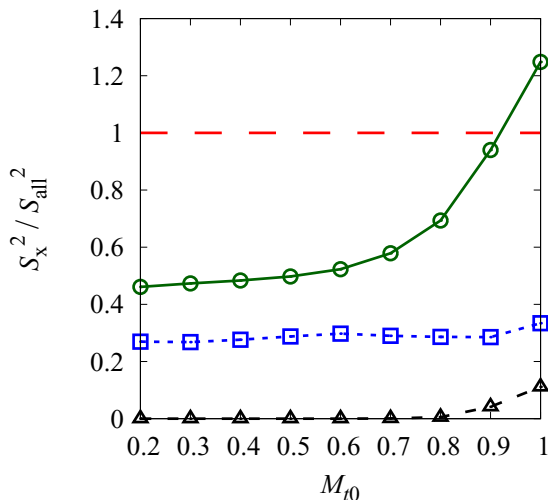


FIG. 5. The ratio of each term to the overall sound source in the sound source strength for $R_{\lambda,0} = 130$: \circ (green), Reynolds stress term S_{Re} ; \square (blue), entropy term S_{en} ; \triangle (black), viscous term S_{vis} . The quantities discussed herein are spatially averaged.

spectra of the term total have two notable characteristics: a decrease in the peak value with increasing turbulent Mach number and the appearance of high wave number components for high turbulent Mach number cases $M_{t0} = 0.8$ – 1.0 . A similar trend is observed in the Reynolds stress term and the entropy term although the degree of change is somewhat different. The peak value decreases more for the entropy term, and the high wave number components increase more for the Reynolds stress term. The decrease in the peak values for the term total, Reynolds stress term, and entropy term can be explained by the compressibility effects in which vortical motion is suppressed [24,45]. The results of the viscous term also replicate the trend in which the values in the high wave number components increase with increasing turbulent Mach number. The appearance of the high wave number components in the high turbulent Mach number cases for all the source terms implies that different sound generation mechanisms exist between low and high turbulent Mach numbers.

The spectra of the terms are compared in Fig. 7. The viscous term is shown only in the figures for the high turbulent Mach number case because the spectra of the viscous term in the low turbulent Mach number case are sufficiently small and do not affect the total spectra. Figure 5 indicates that the Reynolds stress and entropy terms have partially the same signs for low turbulent Mach numbers but opposite signs, in other words, the terms cancel each other out, for high turbulent Mach numbers. Spectra of the Reynolds stress term, the entropy term, and the viscous term are summed up and shown by the dashed-dotted line (yellow), and the contribution to those effects in each scale is discussed. The line does not represent the effects of nullified terms with opposite signs because it only represents the sum of the squared values. If the term total has a smaller value than the simple sum of the spectra, two or all terms have the opposite sign to cancel each other out, and vice versa. In Fig. 7(a) the spectra of the term total show the highest value over the wide range of wave numbers; thus, the Reynolds stress term and the entropy term exhibit the same sign for $M_{t0} = 0.2$. In addition, the spectrum of the entropy term has a peak at a higher wave number than that of Reynolds stress term because the entropy term for low turbulent Mach numbers is generated via viscous effects, as discussed in Sec. III C. In contrast, the spectra of the simple sum of the terms show the highest value for $M_{t0} = 1.0$; thus, either two terms or all terms have different signs. In particular, this trend is remarkable at high wave numbers. These phenomena are caused by shocklets (discussed in detail in Sec. III D). Figure 8 exposes that the probability density functions (PDFs) of the local Mach number $M_{loc} = \sqrt{u_i^2}/c$. For $M_{t0} \geq 0.7$, locally supersonic velocity fluctuations

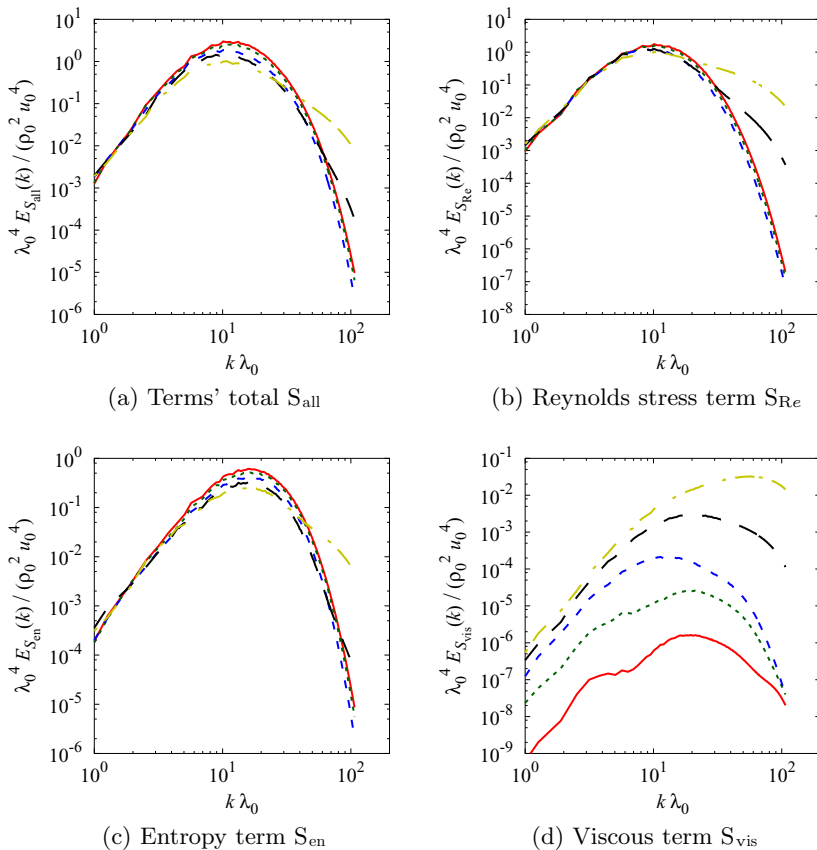


FIG. 6. Sound source spectra of (a) term total S_{all} , (b) Reynolds stress term S_{Re} , (c) entropy term S_{en} and (d) viscous term S_{vis} for $R_{\lambda 0} = 130$: — (red), $M_{t0} = 0.2$; \cdots (green), $M_{t0} = 0.4$; - - (blue), $M_{t0} = 0.6$; - - (black), $M_{t0} = 0.8$; - · - (yellow), $M_{t0} = 1.0$. The values are normalized by the initial values of density ρ_0 , magnitude of velocity u_0 , and Taylor microscale λ_0 .

appear, implying the existence of shocklets. The isosurface of the local Mach number at $M_{\text{loc}} = 1.0$ for $M_{t0} = 1.0$ is shown in Fig. 9, which shows the outer surface of the locally supersonic region. The figure also supports that there exists a certain amount of locally supersonic region, even at the time of a quasi-steady state in which the turbulent Mach number and the Reynolds number decrease compared with those in the initial state.

The relation between the three terms is precisely discussed using the correlation coefficients shown in Table II. Only the high turbulent Mach number cases of $\text{Cor}(S_{\text{Re}}, S_{\text{vis}})$ and $\text{Cor}(S_{\text{en}}, S_{\text{vis}})$ are shown here because the values of viscous terms for low turbulent Mach number cases are negligibly small. The table demonstrates that the Reynolds stress term and entropy term are

TABLE II. Correlation coefficients between three source terms for $R_{\lambda 0} = 130$.

M_{t0}	0.2	0.3	0.4	0.5	0.6	0.7	0.8	0.9	1.0
$\text{Cor}(S_{\text{Re}}, S_{\text{en}})$	0.38	0.36	0.32	0.28	0.22	0.15	0.01	-0.23	-0.44
$\text{Cor}(S_{\text{Re}}, S_{\text{vis}})$	—	—	—	—	—	—	-0.01	-0.08	-0.16
$\text{Cor}(S_{\text{en}}, S_{\text{vis}})$	—	—	—	—	—	—	0.13	0.03	0.02

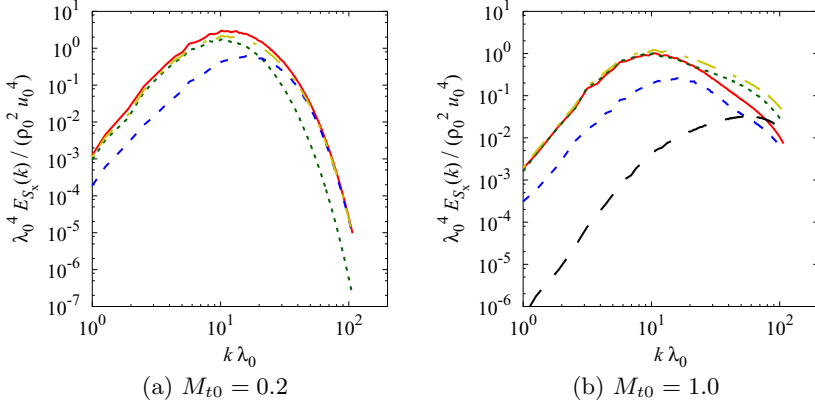


FIG. 7. Sound source spectra for (a) $M_{t0} = 0.2$ and (b) $M_{t0} = 1.0$ at $R_{\lambda 0} = 130$: — (red), term total $E_{S_{\text{all}}}$; \cdots (green), Reynolds stress term $E_{S_{\text{Re}}}$; - - (blue), entropy term $E_{S_{\text{en}}}$; - - (black), viscous term $E_{S_{\text{vis}}}$; - · - (yellow), simple sum of spectra $E_{S_{\text{Re}}} + E_{S_{\text{en}}} + E_{S_{\text{vis}}}$. The viscous term is not shown for $M_{t0} = 0.2$ due to its negligible value. The values are normalized by the initial values of density ρ_0 , magnitude of velocity u_0 , and Taylor microscale λ_0 .

positively correlated in low turbulent Mach numbers and that the correlation becomes negative for high turbulent Mach numbers. The relation of Reynolds stress and entropy terms with the viscous term [$\text{Cor}(S_{\text{Re}}, S_{\text{vis}})$, $\text{Cor}(S_{\text{en}}, S_{\text{vis}})$] does not show any clear correlation. Note that, although the values are small, $\text{Cor}(S_{\text{Re}}, S_{\text{vis}})$ and $\text{Cor}(S_{\text{en}}, S_{\text{vis}})$ decreases with increasing the turbulent Mach numbers. As discussed in Sec. III C, the entropy term is generated by viscous effects, such that the entropy term S_{en} and the viscous term S_{vis} show a positive correlation, whereas the Reynolds stress term S_{Re} and the viscous term S_{vis} do not show clear correlation. The correlation between the entropy term S_{en} and viscous term S_{vis} becomes small for high turbulent Mach number cases (see Sec. III D).

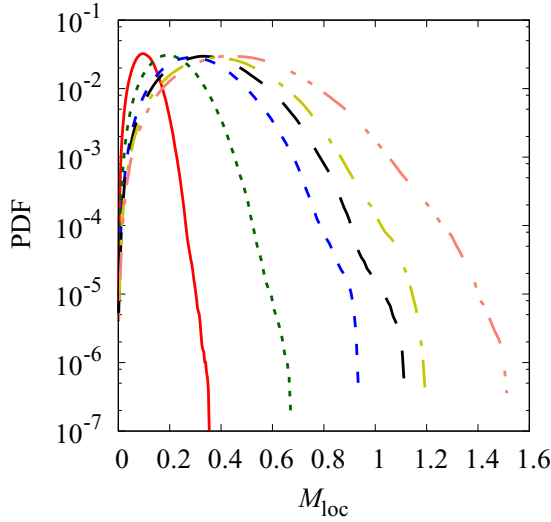


FIG. 8. Probability density functions (PDFs) of the local Mach number at $R_{\lambda 0} = 130$: — (red), $M_{t0} = 0.2$; \cdots (green), $M_{t0} = 0.4$; - - (blue), $M_{t0} = 0.6$; - · - (black), $M_{t0} = 0.7$; - · · - (yellow), $M_{t0} = 0.8$; - · · · - (pink), $M_{t0} = 1.0$.

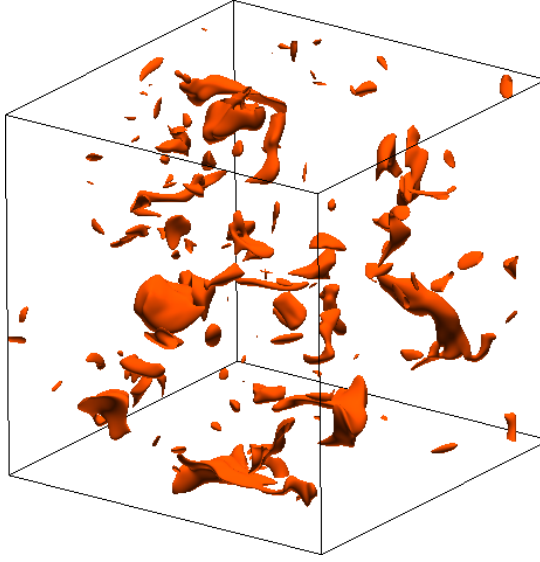


FIG. 9. Isosurface of the local Mach number at $M_{loc} = 1.0$ for $M_{t0} = 1.0$, $R_{\lambda,0} = 130$.

The velocity dependence on the sound source strength is also dependent on the turbulent Mach number. Velocity dependence on acoustic power has been extensively investigated because it is essential for predicting jet noise and designing vehicles [1,2,46]. Figure 10 depicts the velocity dependence on sound source strength for each term. The values are spatially averaged. Three individual source terms indicate that the power law is changed with higher slopes for high turbulent Mach number cases. For low turbulent Mach numbers ($M_{t0} \leq 0.4$), the velocity exponent of the Reynolds stress term, the entropy term, and the viscous term are 3.78, 3.75, and 7.81, respectively. For high turbulent Mach numbers ($M_{t0} \geq 0.9$), the exponents of the terms change to 7.41, 5.88, and 15.9, respectively. For the Reynolds stress term, S_{Re} , the exponent of fourth corresponds to Lighthill's power law of eighth for sound pressure level. Here, the exponent of 4 is derived without considering the propagation effects because this discussion focuses on the sound source rather than the acoustic wave. The slope of the term total, however, does not change much from 3.72. These behaviors should be explained by the change of the mechanisms in the low and high turbulent Mach number cases. In low turbulent Mach number cases, the sound source terms are generated only by vortical motion; however, in high turbulent Mach number cases, ($M_{t0} \geq 0.7$), eddy shocklets largely contribute to the generation of the source terms. This leads to the changes in the exponent of the slope for the three individual source terms. The slope of the term total does not change considerably for the high turbulent Mach number cases because the Reynolds stress term and the entropy term show opposite signs across shocklets in high turbulent Mach number cases (see Sec. III D) and hence cancel each other out. Again, the discussion above does not exactly correspond to previous research [1,2,46] because our investigation focuses on the sound source strength (not acoustic power in far fields). However, we believe that the information provided herein will facilitate the discussion of the velocity dependence of the acoustic power in far fields, particularly for high turbulent Mach number flows.

In summary, the results exhibit the different sound source characteristics between the low and high turbulent Mach number flows. The following subsections discuss the detailed characteristics of sound sources for the low and high turbulent Mach number cases. $M_{t0} = 0.2$ and $M_{t0} = 1.0$ are selected to represent the low and high turbulent Mach number cases, respectively. In the next subsection, the sound source characteristics in the low turbulent Mach numbers are discussed in

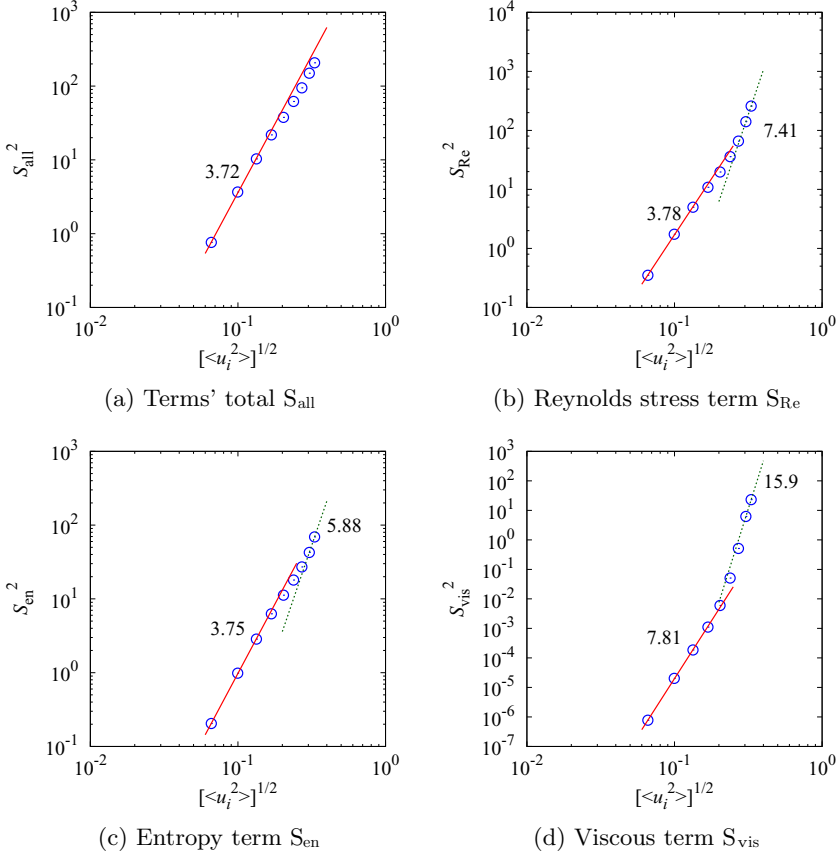


FIG. 10. Velocity dependence on sound sources of (a) term total S_{all} , (b) Reynolds stress term S_{Re} , (c) entropy term S_{en} , and (d) viscous term S_{vis} for $R_{\lambda 0} = 130$.

detail; then, the detailed characteristics of the high turbulent Mach number cases are investigated in the following subsection.

C. Sound sources at low turbulent Mach numbers

Figure 5 shows that the Reynolds stress term and the entropy term are two main sound source terms in low turbulent Mach numbers; thus, those terms are analyzed herein. First, we discuss the Reynolds stress term by focusing on its similarity with the second invariant of the velocity gradient tensor. Choi *et al.* [28] showed that the coherent fine-scale structures [47–49] extracted by positive value of the second invariant of the velocity gradient tensor (expressing rotational flow region) has close connection to the generation of Reynolds stress and entropy terms. Also, in the incompressible limit, the Reynolds stress term and the second invariant of the velocity gradient tensor are exactly the same. Thus, the difference between those two in the higher turbulent Mach numbers is given by the compressibility effects. The second invariant of the velocity gradient tensor is defined as

$$Q = \xi_1 \xi_2 + \xi_2 \xi_3 + \xi_3 \xi_1 = \frac{1}{2}(P^2 - S_{ij}S_{ij} + \Omega_{ij}\Omega_{ij}), \quad (13)$$

where $P = -(\xi_1 + \xi_2 + \xi_3) = -\partial u_i / \partial x_i = -\theta$, $S_{ij} = 1/2(\partial u_i / \partial x_j + \partial u_j / \partial x_i)$ and $\Omega_{ij} = 1/2(\partial u_i / \partial x_j - \partial u_j / \partial x_i)$ are the first invariant of the velocity gradient tensor (negative dilatation), the strain rate tensor and the rotation rate tensor, respectively, and ξ_i are the three eigenvalues of the velocity gradient tensor. In the incompressible limit, P is negligible due to the divergence free flow

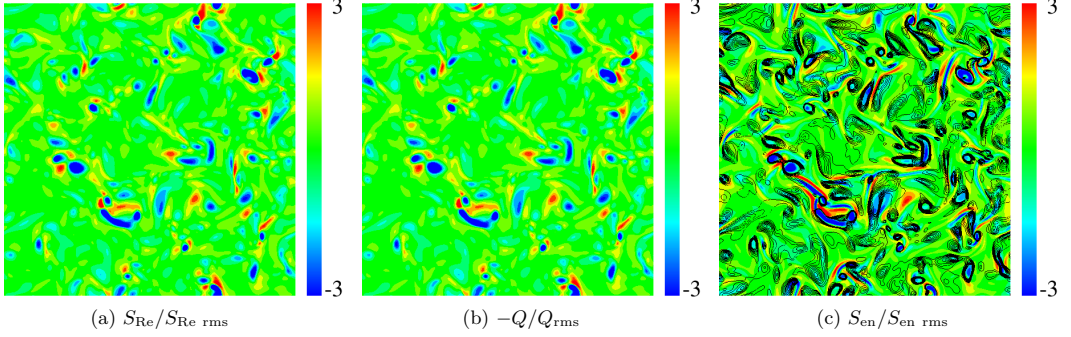


FIG. 11. Cross sections of (a) normalized Reynolds stress term $S_{Re}/S_{Re\ rms}$, (b) normalized negative second invariant $-Q/Q_{rms}$, and (c) normalized entropy term $S_{en}/S_{en\ rms}$ at $z/2\pi = 0.5$. Note that entropy term, $S_{en}/S_{en\ rms}$, is shown with contour lines of the normalized second invariant Q/Q_{rms} . The range of contour lines is $0 \leq Q/Q_{rms} \leq 2$.

field; thus, Eq. (13) can be written as follows:

$$Q = Q_{inc} = \frac{1}{2}(-S_{ij}S_{ij} + \Omega_{ij}\Omega_{ij}) = -\frac{1}{2} \frac{\partial u_i}{\partial x_j} \frac{\partial u_j}{\partial x_i}. \quad (14)$$

Then, assuming constant density, the Reynolds stress term in the incompressible limit is written as

$$\begin{aligned} S_{Re\ inc} &= \rho_\infty \frac{\partial^2(u_i u_j)}{\partial x_i \partial x_j} \\ &= \rho_\infty \frac{\partial}{\partial x_j} \left(\frac{\partial u_i u_j}{\partial x_i} \right) \\ &= \rho_\infty \frac{\partial}{\partial x_j} \left(u_i \frac{\partial u_j}{\partial x_i} + u_j \frac{\partial u_i}{\partial x_i} \right) \\ &\simeq \rho_\infty \frac{\partial}{\partial x_j} \left(u_i \frac{\partial u_j}{\partial x_i} \right) \\ &= \rho_\infty \frac{\partial u_i}{\partial x_j} \frac{\partial u_j}{\partial x_i} + \rho_\infty u_i \frac{\partial}{\partial x_i} \left(\frac{\partial u_j}{\partial x_j} \right) \\ &\simeq \rho_\infty \frac{\partial u_i}{\partial u_j} \frac{\partial u_j}{\partial x_i}, \end{aligned} \quad (15)$$

where $\partial x_k / \partial u_k \simeq 0$ is adopted to the fourth and sixth equalities in Eq. (15). Equations (14) and (15) show that the second invariant and the Reynolds stress term indicate almost the same distributions each other (but signs are opposite) in the low Mach number flows, as shown in Choi *et al.* [28]. The Reynolds stress term and the negative second invariant of the velocity gradient tensor for $M_{t0} = 0.2$ is shown in Fig. 11. Both show almost the same distributions, as expected. In addition, the correlation coefficients of the Reynolds stress term and the negative second invariant $\text{Cor}(S_{Re}, -Q)$ for $M_{t0} = 0.2$ is 0.99. Thus, only vortical motions contribute to generate the Reynolds stress term of the sound sources in the low turbulent Mach number cases.

Recalling the results of Fig. 5, the assumption of the isentropic flow is not applicable due to the existence of the entropy term. Figure 11(c) shows that the nonnegligible entropy term appears around and on the second invariant of the velocity gradient tensor (and so the Reynolds stress term), which makes a positive correlation between the Reynolds stress and entropy terms as shown in

Table II. The reason is discussed hereafter. Recalling that the entropy difference ds is written as

$$\frac{ds}{c_v} = \frac{dp}{p} - \gamma \frac{d\rho}{\rho}, \quad (16)$$

where c_v is the specific heat at constant volume. Also, if we consider two spacial points difference of the entropy component of the Lighthill's turbulent stress tensor in nondimensional form [see Eq. (11)] is

$$\begin{aligned} \Delta T_{\text{en}} &= \Delta p - \Delta \rho \\ &= \frac{\rho_\infty}{\gamma} \left(c_\infty^2 \frac{\Delta p}{p_\infty} - \gamma \frac{\Delta \rho}{\rho_\infty} \right) \\ &= \frac{\rho_\infty}{\gamma} \left(\frac{\Delta p}{p_\infty} - \gamma \frac{\Delta \rho}{\rho_\infty} \right). \end{aligned} \quad (17)$$

Here $c_\infty^2 = \gamma p_\infty / \rho_\infty = 1$ is used for the last equality, because the equations are nondimensionalized with the speed of sound c . Since c_v in Eq. (16) is constant in the present simulation, Eqs. (16) and (17) indicate that the generation of entropy s and entropy component of the Lighthill's turbulent stress tensor T_{en} (&entropy term S_{en}) is almost identical. In addition, the flow is low turbulent Mach number and unheated. Therefore, the entropy generation is governed by the viscous effects, and the heat conduction [1,50]. It is confirmed with the following entropy equation;

$$\rho T \left(\frac{\partial s}{\partial t} + (\nabla \cdot \mathbf{u})s \right) = \frac{M}{\text{Re}} \left(-\frac{\partial q_j}{\partial x_j} + \varepsilon \right), \quad (18)$$

where the heat flux vector q_i and the dissipation ε are defined as

$$\begin{aligned} q_i &= -\kappa \frac{\partial T}{\partial x_i} \\ &= -\frac{\mu}{\text{Pr}(\gamma - 1)} \frac{\partial c^2}{\partial x_i}, \\ \varepsilon &= \sigma_{ij} \frac{\partial u_i}{\partial x_j}. \end{aligned}$$

The equation shows that the heat conduction term is related with viscosity, too. Besides, since in unheated flows, the order of viscous effects and heat conduction are the same [50], it can be said that the viscous effects cause the entropy generation in unheated flows. It is also supported by Choi *et al.* [28] that they showed that the dissipation contributes to generate entropy term in the low convective Mach number mixing layer. Thus, the nonnegligible entropy term occurs due to the limited Reynolds number we investigated. The results show that there is a case that the Reynolds number is high enough for negligible contribution from the viscous term S_{vis} , but not high enough for neglecting the entropy term S_{en} . Furthermore, the fact that the entropy term is generated by viscous effects (caused by vortical motion) supports the positive correlation between the Reynolds stress and entropy terms in low turbulent Mach number flows as shown in Table II.

Finally, the Reynolds number dependence for the overall characteristic of source terms is discussed. The change in the characteristics depending on the Reynolds number is explained by using sound source spectra for three different Reynolds number cases in Fig. 12. Note that the viscous term is not shown here due to its negligible value. The larger peak values and high wave number components appear with increasing the Reynolds number, but the basic shape of spectra does not change for all the terms. These results are reasonable because the characteristics correspond to those of the high Reynolds number flows.

Since the entropy term is generated with viscous effects as discussed above, the Reynolds number dependence on the overall entropy term strength (corresponding to the integral of the entropy term

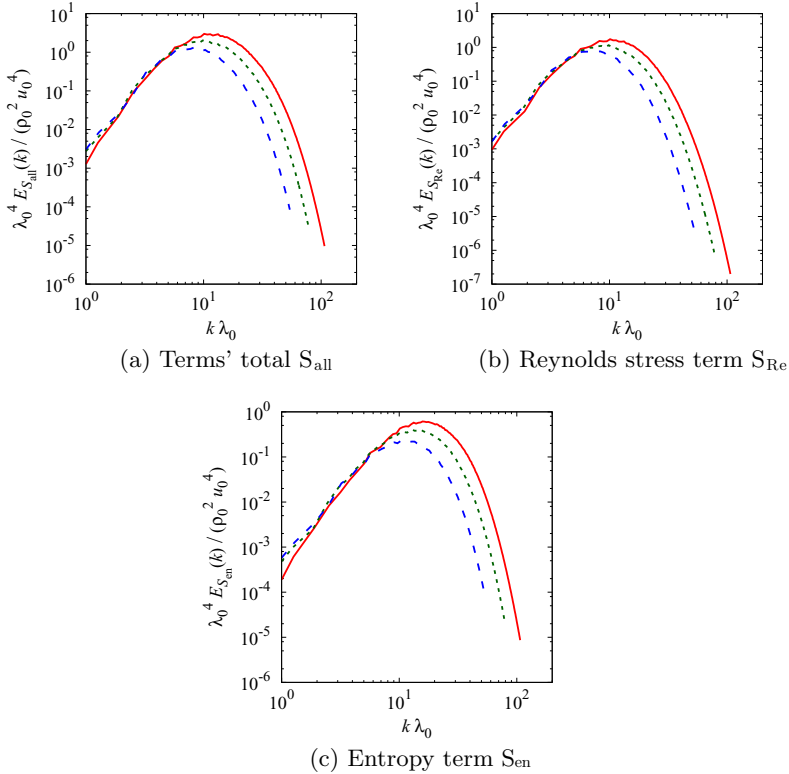


FIG. 12. Reynolds number dependence on sound source spectra of (a) term total, S_{all} , (b) Reynolds stress term, S_{Re} , and (c) entropy term, S_{en} , for $M_{I0} = 0.2$: — (red), $R_{\lambda,0} = 130$; - - (green), $R_{\lambda,0} = 100$; - - (blue), $R_{\lambda,0} = 70$.

spectra) should be discussed. Figure 13 shows the Reynolds number dependence of the contributions of each source term. All Reynolds number cases show the nonnegligible contribution of the entropy term. In addition, the entropy contribution rather slightly increases with increasing the Reynolds number. From Eq. (18), the magnitude of the entropy generation is determined by two factors: (1) the Reynolds number and (2) the change in flow. In the Reynolds number we investigated, the intensification of the entropy generation by the change in the flow is larger than that of the reduction of entropy generation by the Reynolds number increase. The trend that the entropy term spectra have the larger peak and the higher wave number components with increasing the Reynolds number in Fig. 12(c) supports the discussion above. However, in the higher Reynolds number than that of the present simulation, the trend would be changed due to less viscosity, and the entropy term would become negligible.

D. Sound sources at high turbulent Mach numbers

In low turbulent Mach numbers, the Reynolds stress term and the second invariant of the velocity gradient tensor show almost the same distributions. In addition, the entropy term appears on the second invariant and its surroundings. These results demonstrate that the vortices contribute to sound generation in the cases with low turbulent Mach numbers. However, it would be changed, because the similarity between the Reynolds stress term and the second invariant of the velocity gradient tensor brakes due to its compressibility in the high turbulent Mach number flows. Figures 14(a) and 14(b) show the cross section of the Reynolds stress term and the negative second invariant of the

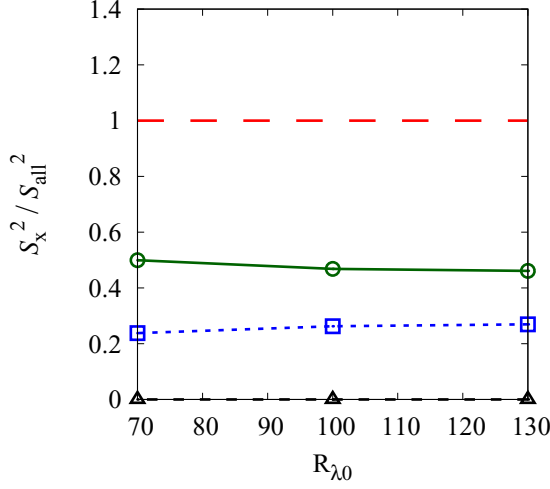


FIG. 13. The ratio of each term to the overall sound source in the sound source strength for $M_{t0} = 0.2$: ○ (green), Reynolds stress term S_{Re} ; □ (blue), entropy term S_{en} ; △ (black), viscous term S_{vis} . The quantities discussed herein are spatially averaged.

velocity gradient tensor, respectively. Note that, in Fig. 14(b), we employ the second invariant in the incompressible limit [Eq. (14)] for the visualization. This is because we focus on the rotational motion of vortices. Though the effects of the dilatational component, $P = -(\xi_1 + \xi_2 + \xi_3) = -\partial u_i / \partial x_i = -\theta$, in the second invariant is negligibly small in low turbulent Mach numbers, the effects cannot be negligible in cases with high turbulent Mach numbers. Figures 14(a) and 14(b) show that the Reynolds stress term and the negative second invariant have similar features, but the correlation between the Reynolds stress term and the negative second invariant is smaller than that for the low turbulent Mach numbers. The correlation coefficient of the Reynolds stress term and the negative second invariant, $\text{Cor}(S_{\text{Re}}, -Q_{\text{inc}})$, changes from 0.99 for $M_{t0} = 0.2$ to 0.51 for $M_{t0} = 1.0$.

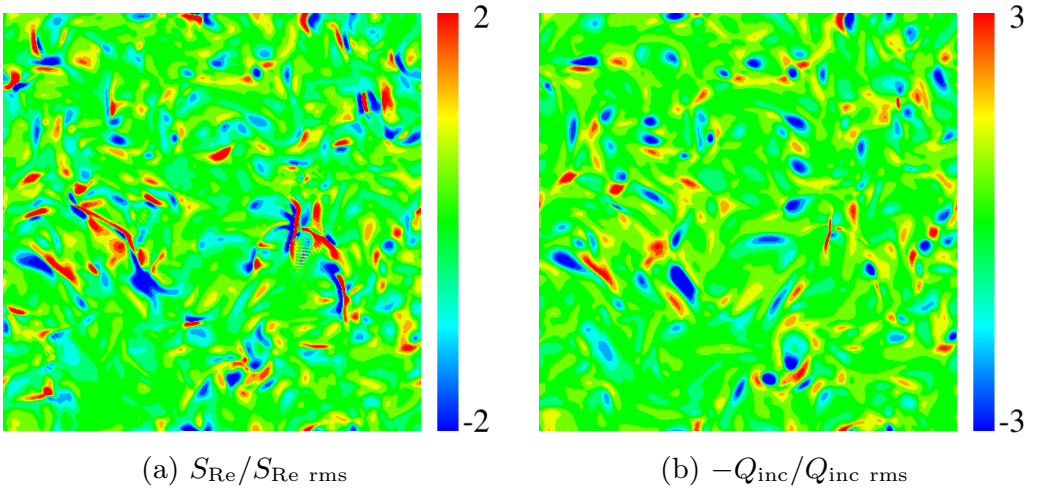


FIG. 14. Cross sections of (a) normalized Reynolds stress term, $S_{\text{Re}} / S_{\text{Re rms}}$ and (b) normalized negative second invariant in the incompressible limit, $-Q_{\text{inc}} / Q_{\text{inc rms}}$ at $z/2\pi = 0.5$.

TABLE III. Corelation coefficients between Reynolds stress term, S_{Re} , and entropy term, S_{en} , with various dilatation levels for $M_{t0} = 1.0$, $R_{\lambda,0} = 130$.

θ/θ_{rms}	$[-\infty, -2.0]$	$[-2.0, -1.0]$	$[-1.0, 0.0]$	$[0.0, 1.0]$	$[1.0, 2.0]$	$[2.0, \infty]$
$Cor(S_{Re}, S_{en})$	-0.80	-0.44	-0.22	-0.14	-0.21	-0.43

For the characteristics of the source terms, Table II shows that the Reynolds stress term and the entropy term in high turbulent Mach numbers have a negative correlation, whereas they have a positive correlation in low turbulent Mach numbers. An important difference between low turbulent Mach number and high turbulent Mach number flows is the level of dilatation. The level of dilatation increases due to the compressibility for high turbulent Mach numbers. Previous studies [27,41,51] conducted conditional sampling by the local dilatation level and exhibited that the statistical properties in the strong compression region are altered significantly due to the existence of shocklets. We follow their analysis and apply it to sound source terms. Table III shows correlation coefficients between the Reynolds stress and the entropy terms based on various dilatation levels. The results show that strong negative correlation appears in the strong compression region, $\theta/\theta_{rms} \leq -2$. In addition, in Table IV, the strong compression region is the dominant contributor to the overall sound source strength for the Reynolds stress and the entropy terms. Note that $Cor(S_{Re}, S_{en})$ shows negative values in all the regions, though the magnitude is not substantially large compared with the strong compression region, $\theta/\theta_{rms} \leq -2$. Recalling that low turbulent Mach numbers produce a positive correlation between the Reynolds stress and the entropy terms, the results indicate that the sound source structures are significantly changed by the existence of shocklets. It should be noted, however, that the contribution of vortical motion to the sound source still exists because the peak wave number in the spectra of the Reynolds stress and entropy terms in Figs. 6(b) and 6(c) are kept around $k\lambda_0 = 100$ for $M_{t0} = 1.0$ and are not changed significantly from the low turbulent Mach number case of $M_{t0} = 0.2$ in which sound sources are generated by vortical motion. Also, in $\theta/\theta_{rms} \leq -2$, the viscous term has a large magnitude affected by shocklets, which results in nonnegligible contributions to the overall sound source distributions for high turbulent Mach numbers (see Fig. 5). These results suggest that the emergence of important sound sources caused by the strong compression event of shocklets precipitates a negative correlation between the Reynolds stress and the entropy terms. The isosurfaces of dilatation at $\theta/\theta_{rms} = -3$ colored by the Reynolds stress term and the entropy term are visualized in Fig. 15. Isosurfaces of dilatation which appears in the vicinity of the locally supersonic region in Fig. 9 show sheetlike structures of shocklets reported by Wang *et al.* [27]. Also, both terms show large values on the isosurface of dilatation. In addition, the distributions of the Reynolds stress term and the entropy term seem to show opposite signs, which is confirmed later in Fig. 16 where sound source distributions across shocklets are extracted. Therefore, shocklets in strong compression regions become sound sources, thereby canceling the Reynolds stress and entropy terms each other out.

In order to discuss the contributions of shocklets to sound sources in detail, shocklet extraction is conducted. The method used here is similar to that used in previous studies [23,26,37]. The

 TABLE IV. Percentage of sound source strength in flow regions with various dilatation levels for $M_{t0} = 1.0$, $R_{\lambda,0} = 130$.

θ/θ_{rms}	$[-\infty, -2.0]$	$[-2.0, -1.0]$	$[-1.0, 0.0]$	$[0.0, 1.0]$	$[1.0, 2.0]$	$[2.0, \infty]$
Fractions of S_{all}^2 [%]	26.4	10.0	24.4	29.0	8.0	2.2
Fractions of S_{Re}^2 [%]	48.7	9.5	17.0	18.0	5.2	1.6
Fractions of S_{en}^2 [%]	30.1	8.4	23.2	29.0	7.5	1.8
Fractions of S_{vis}^2 [%]	75.7	5.0	5.2	5.0	3.9	5.2

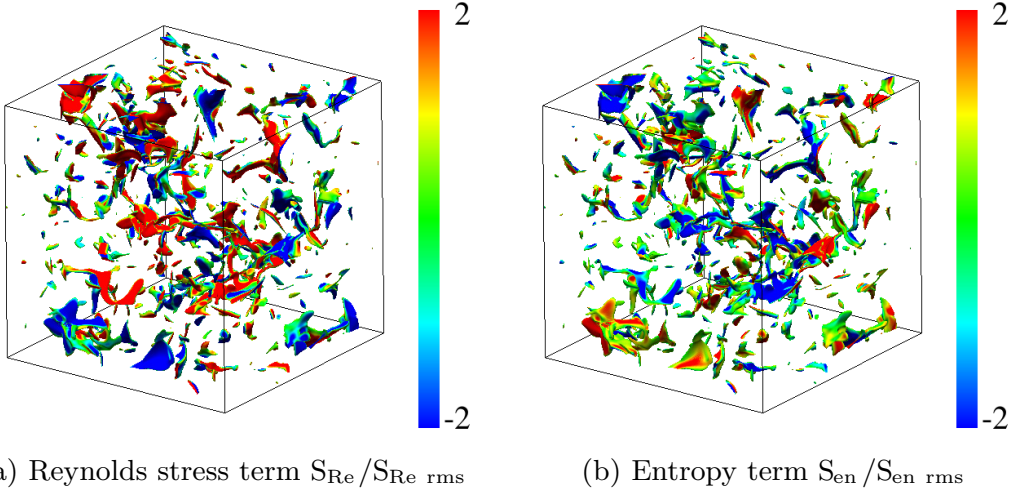


FIG. 15. Distributions of (a) normalized Reynolds stress term, $S_{Re}/S_{Re\ rms}$, and (b) normalized entropy term, $S_{en}/S_{en\ rms}$, on the isosurface of normalized dilatation $\theta/\theta_{rms} = -3$.

procedure is written in the Appendix. The sound sources around shocklets are then discussed in detail using the extracted shock waves. Figure 16 displays the sound source distributions across shocklets for $R_{\lambda 0} = 130$, $M_{t0} = 1.0$. All the terms have large values near shocklets. The term total, S_{all} , and the Reynolds stress term, S_{Re} , have similar shapes (negative and positive peaks at the front and back sides of the shocklets, respectively), hence the Reynolds stress term is the main sound source term across shocklets. The entropy term also has two peaks across the shocklets, but the sign is opposite to that of the Reynolds stress term. These results indicate that the Reynolds stress term and the entropy term cancel each other out across shocklets. The viscous term, on the other hand, has

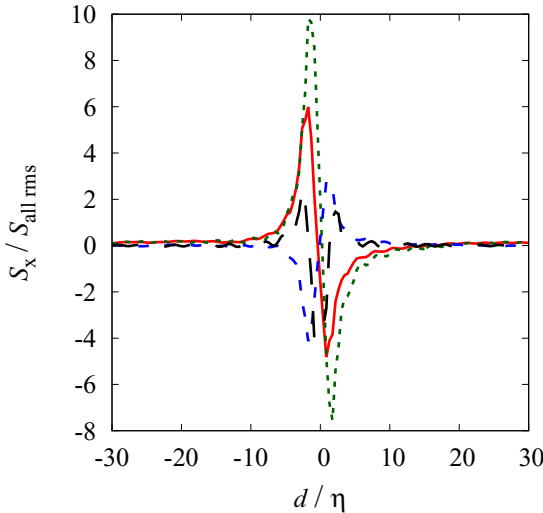


FIG. 16. Sound source distributions across shocklets for $M_{t0} = 1.0$, $R_{\lambda 0} = 130$: — (red), term total S_{all} ; \cdots (green), Reynolds stress term S_{Re} ; - - (blue), entropy term S_{en} ; - - (black), viscous term S_{vis} . The values are normalized by the rms value of the term total, $S_{all\ rms}$. The positive and the negative d show the upstream and the downstream of the shocklets, respectively.

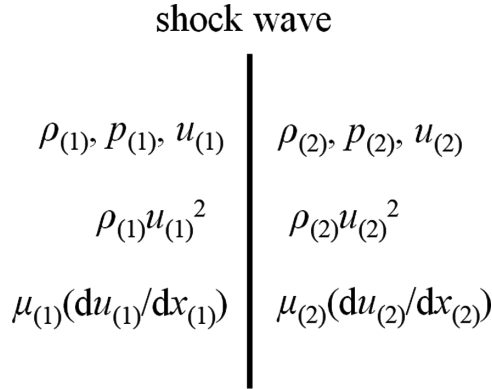


FIG. 17. Schematic of physical quantities across the one-dimensional shock. (1) is the upstream, and (2) is the downstream values, respectively.

a different trend with a strong negative peak at the position of the shocklets and two positive peaks at the front and the back sides of the shocklets. To summarize, the Reynolds stress term and the entropy term show opposite signs and the viscous term displays a different trend; these trends can be explained using a one-dimensional shock relation with Lighthill's turbulent stress tensor shown in Eq. (11). Let the subscripts (1) and (2) be the upstream and the downstream values of a shock, respectively, as shown in Fig. 17. In one dimension, the Reynolds stress component of Lighthill's turbulent stress tensor is written as ρu^2 . The mass conservation law, $\rho_{(1)}u_{(1)} = \rho_{(2)}u_{(2)}$, leads to a solution that the ratio of the Reynolds stress component across a shock is the same as that of the velocity (i.e. $\rho_{(1)}u_{(1)}^2/\rho_{(2)}u_{(2)}^2 = u_{(1)}/u_{(2)}$). Also, the ratio of the entropy component of the Lighthill's turbulent stress tensor in nondimensional form across a shock is determined as follows:

$$\begin{aligned}
 \frac{T_{\text{en}(2)}}{T_{\text{en}(1)}} &= \frac{P_{(2)} - \rho_{(2)}}{P_{(1)} - \rho_{(1)}} \\
 &= \frac{\frac{\rho_{(2)}}{\rho_{(1)}}P_{(1)} - \frac{\rho_{(2)}}{\rho_{(1)}}\rho_{(1)}}{P_{(1)} - \rho_{(1)}} \\
 &> \frac{\frac{\rho_{(2)}}{\rho_{(1)}}(P_{(1)} - \rho_{(1)})}{P_{(1)} - \rho_{(1)}} \\
 &> 1,
 \end{aligned} \tag{19}$$

where $p_{(2)}/p_{(1)} > \rho_{(2)}/\rho_{(1)}$ and $\rho_{(2)}/\rho_{(1)} > 1$ are used for the third and fourth inequalities. Equation (19) shows that the change direction in the entropy component is the same as that of density. In one-dimensional shock relation, the change in density is the opposite to that of the velocity across a shock (coming from $\rho_{(1)}/\rho_{(1)} = u_{(1)}/u_{(2)}$). Thus, the change in the Reynolds stress component (the ratio of which is the same as that of velocity) is the opposite that of the density, and entropy component across a shock. In addition, the viscous component in one dimension is written as $\mu \partial u / \partial x$. As the change in μ across shocklets is small compared to that of the first derivative of the velocity, the viscosity is assumed to be constant across a shock. Thus, the distribution of the viscous component corresponds to that of the first derivative of the velocity. The discussion above expresses that the ratio of the change in the Reynolds stress component across a shock is similar to that of the velocity. Thus, the first derivative of the Reynolds stress term distribution in Fig. 16 is similar to that of the viscous term. The positive slope at the front and back of shocklets and the negative slope near shocklets are observed in the distribution of the Reynolds stress term. If the first derivative of the distribution is considered, two positive peaks at the front and back of the shocklets and one negative peak near the center of shocklets are derived for the viscous

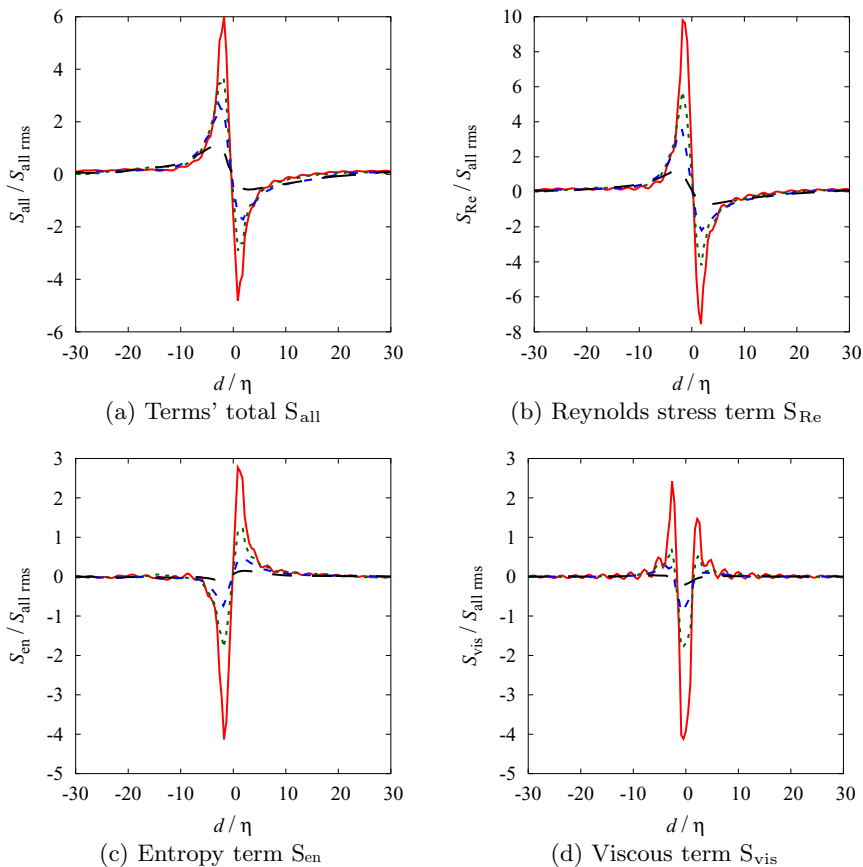


FIG. 18. Turbulent Mach number dependence on sound sources across shocklets for $R_{\lambda,0} = 130$: — (red), $M_{t0} = 1.0$; \cdots (green), $M_{t0} = 0.9$; - - (blue), $M_{t0} = 0.8$; - · - (black), $M_{t0} = 0.7$. (a) Term total S_{all} , (b) Reynolds stress term S_{Re} , (c) entropy term S_{en} , and (d) viscous term S_{vis} . The values are normalized by the rms value of the term total, $S_{\text{all rms}}$. The positive and the negative d show the upstream and downstream of the shocklets, respectively.

term distribution. The distribution of the viscous term in Fig. 16 supports the explanation above. Finally, the dependence of the turbulent Mach number and the Reynolds number on sound sources across shocklets are investigated. Figure 18 exhibits the sound source distributions across shocklets with four different turbulent Mach numbers. All the terms show larger values with increasing the turbulent Mach numbers due to the appearance of stronger shocklets in high turbulent Mach number cases. The Reynolds number dependence is also shown in Fig. 19. The trend is the same as that of the turbulent Mach number. Larger Reynolds numbers show larger values of sound sources. Lee *et al.* [22] explained that higher Reynolds numbers lead to more frequent large-compression events of shocklets. Though the difference between $R_{\lambda,0} = 70$ and $R_{\lambda,0} = 100$ is small, our results also show the appearance of stronger shocklets with increasing Reynolds numbers, as seen in Fig. 20. Therefore, the high Reynolds numbers also cause stronger shocklets, and subsequently, stronger sound sources are created. Note that the contribution of the viscous term is expected to become smaller for high Reynolds number flows, but our results do not demonstrate the smaller viscous term with increasing the Reynolds number due to the limited Reynolds number range in the present computation.

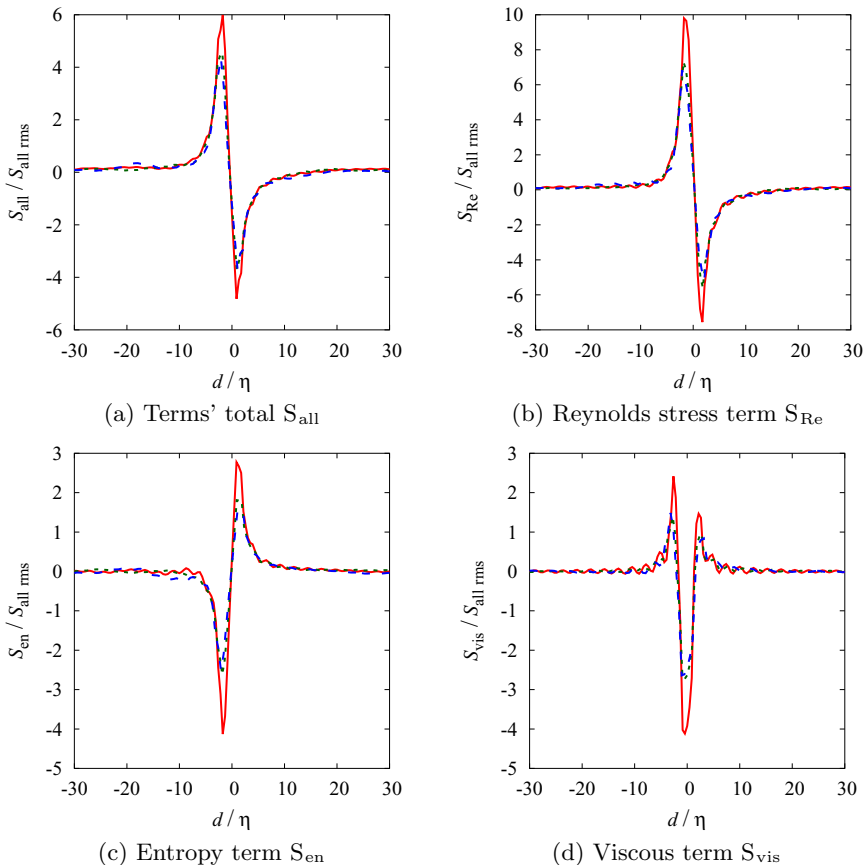


FIG. 19. Reynolds number dependence on sound sources across shocklets for $M_{t0} = 1.0$: — (red), $R_{\lambda 0} = 130$; \cdots (green), $R_{\lambda 0} = 100$; - - (blue), $R_{\lambda 0} = 70$. (a) Term total, S_{all} , (b) Reynolds stress term, S_{Re} , (c) entropy term, S_{en} , and (d) viscous term, S_{vis} . The values are normalized by the rms value of the term total, $S_{\text{all rms}}$. The positive and negative d show the upstream and downstream of shocklets, respectively.

E. Discussion

In the previous subsections, it has been shown that shocklets become key sound sources in high turbulent Mach number flows. In order to elucidate the applicability of the given results to the real flow applications, we discuss the two important topics (1) the extension to the far-field acoustic wave prediction and (2) the connection of the present results with the crackle noise mechanism.

1. Extension to the far-field acoustic wave prediction

The present paper does not discuss far-field acoustic waves directly, but discusses the sound source itself. Therefore, we should mention the relationship between the present results and far-field acoustic waves and make clear the applicability and the limitation of the present paper. In order to elucidate the discussion points, four important topics: (a) cancellation, (b) mean flow interaction, (c) nonlinear propagation effects, and (d) effects of enthalpy and type of sources which determine far-field acoustic wave characteristics are selected and discussed.

a. Cancellation. Although the sound source characteristics have been focused on throughout this article, some researchers would argue that not all the pressure waves generated by sound sources do not propagate to the far-field due to cancellation in propagation [50]. We believe, however,

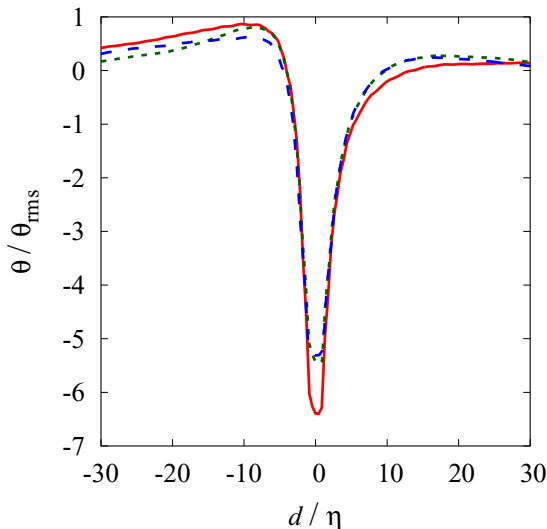


FIG. 20. Distribution of normalized dilatation, $\theta / \theta_{\text{rms}}$, across shocklets for $M_{i0} = 1.0$: — (red), $R_{\lambda 0} = 130$; \cdots (green), $R_{\lambda 0} = 100$; - - (blue), $R_{\lambda 0} = 70$. The positive and the negative d show the upstream and downstream of shocklets, respectively.

that the given results in the present paper are still helpful to understand the sound generation mechanism for the high turbulent Mach number flows for the following reasons. First, as shown in Sec. III D, shocklets that have unsteady and intermittent characteristics are key sound sources in the high turbulent Mach number flows. The unsteady and intermittent characteristics of shocklet (and generated acoustic waves) decrease the possibility of the canceling in propagation. In fact, the strong unsteady, intermittent phenomenon has been shown to become strong sound sources in the potential core for the compressible jets [52,53]. In addition, another work on DNS of temporally evolving mixing layer by the present authors showed that the generation of shocklets affects the shape of pressure spectra in at least near field (see more detailed explanation in Sec. III E 2). Finally, it should be noted that the sound source characteristics have been discussed with properly processed statistics of sound source terms, such that completely random phenomena making cancellation are excluded from the discussion in the present paper.

b. Mean flow interaction. The nonuniform mean flow in the vicinity of the sound source would affect the radiated acoustic wave characteristics and it is not taken into account in the original form of the Lighthill equation [50]. As the effects are described by nonlinear terms, we would need to use a higher wave equation in the moving frame as proposed by Phillips [54] and Lilley [55] (quoted in [56]). The objective of the present paper, however, is not to understand the effects of mean flow interaction, but to understand the sound source characteristics in high turbulent Mach number or high turbulent fluctuation flows, and thus, isotropic turbulence is selected for this study. In isotropic turbulence, the mean flow does not exist, such that the generated acoustic waves are not affected by mean flow. Therefore, it is not necessarily to use higher-order (and complicated) wave equations, and the Lighthill equation is sufficient to analyze the sound source characteristics in terms of the effects of turbulent Mach number. In addition, we believe that the simplest study approach with isotropic turbulence and the Lighthill equation can be helpful to focus on the effects of turbulent Mach number or turbulent fluctuation on sound source characteristics.

c. Nonlinear propagation effects. For high Mach number supersonic jets, it has been observed that the far-field acoustic waves show distinguished high wave number components in the spectra and N-shaped waveform, which are known as nonlinear propagation effects [12–15]. The original form of the Lighthill equation is based on the linear wave equation, and thus, the equation can

not deal with the nonlinear propagation effects. Our scope of the present paper is, however, not to understand the effects of nonlinearity in propagation, but to understand the sound source characteristics. Based on the Lighthill equation, Miller [29] proposed a nonlinear acoustic analogy in which far-field acoustic waves are predicted with the combination of sound source spectra given by the Lighthill's acoustic analogy and Burgers' equation. Our results can be helpful for the modeling of sound source spectra. From our results, at least, the Reynolds stress component and entropy component of Lighthill's turbulent stress tensor needs to be correctly considered in the modeling of sound source spectra in the high turbulent Mach number flows, because those terms are canceled each other out across shocklets; important sound sources in high turbulent Mach numbers. In addition, it is worth noting that nonlinear propagation effects are small for near-field acoustic wave characteristics [12–15] and the study with the Lighthill equation is useful for understanding the sound source characteristics of near-field acoustic waves as well.

d. Effects of enthalpy and type of sources. Lilley [57] discussed the effects of enthalpy and the type of sources by deforming the entropy term in the Lighthill equation toward the application of low Mach number heated jets. The Lilley's decomposition of the Lighthill's turbulent stress tensor (rearranged by Bodony and Lele [58]) in nondimensional form is written as follows:

$$T_{ij} = \rho u_i u_j - \frac{\gamma - 1}{2} \rho u_k u_k \delta_{ij} + \int \frac{\partial}{\partial x_k} \left[\rho u_k \left(\frac{h_\infty - h_s}{h_\infty} \right) \right] \delta_{ij} dt + \frac{M}{\text{Re}} \sigma_{ij}. \quad (20)$$

Based on Lilley's decomposition, the sound source terms in the Lighthill equation is written in the following form:

$$\begin{aligned} S_{\text{mom}} &= \frac{\partial^2 (\rho u_i u_j - \frac{\gamma-1}{2} \rho u_k u_k \delta_{ij})}{\partial x_i \partial x_j}, \\ S_{\text{enth}} &= \frac{\partial^2 (\int \frac{\partial}{\partial x_k} [\rho u_k (\frac{h_\infty - h_s}{h_\infty})] \delta_{ij} dt)}{\partial x_i \partial x_j}, \\ S_{\text{vis}} &= \frac{\partial^2 (\frac{M}{\text{Re}} \sigma_{ij})}{\partial x_i \partial x_j}, \\ S_{\text{all}} &= S_{\text{mom}} + S_{\text{enth}} + S_{\text{vis}}, \end{aligned} \quad (21)$$

where S_{mom} is the momentum term, S_{enth} is the enthalpy term, and S_{vis} is the viscous term, respectively. He showed that the enthalpy fluctuation having dipole source characteristics becomes more important than the quadruple source based on momentum stress term in hot subsonic jets. A following study shows that the characteristics retain in heated supersonic jets [58]. Figure 21 shows that sound source distributions in Lilley's decomposition, where enthalpy term is computed by subtracting a part of momentum term $-(\gamma - 1)/2 \rho u_k u_k \delta_{ij}$ from the entropy term S_{en} [see Eqs. (21) and (12)]. Figure 21 shows that the momentum term; quadruple source is dominant across shocklets, and the enthalpy term; dipole source is less important. Since the momentum term shows that it is the largest value and the distribution is similar to that of overall sound source. Thus, we conclude that the generated sources by shocklets show quadruple characteristics at least in unheated high turbulent Mach number flows.

2. Connection of present results with crackle noise

In the introduction, we mention that previous studies suggested that turbulent fluctuation can be a key to generating crackle noise and one of our targets is to find a clue for the contribution to the generation mechanisms from the fine-scale turbulence. Although, recent papers [19,20] showed that the change of the large-scale turbulent structure generated intense Mach wave leading to skewed acoustic wave $S(p) > 0.4$ which has been widely used as a criterion for the crackle. However, we should mention two unresolved points for the crackle noise. First, the criterion of $S(p) > 0.4$ is an empirical or adhoc criterion given by the experimental results, and thus, it could not represent all the

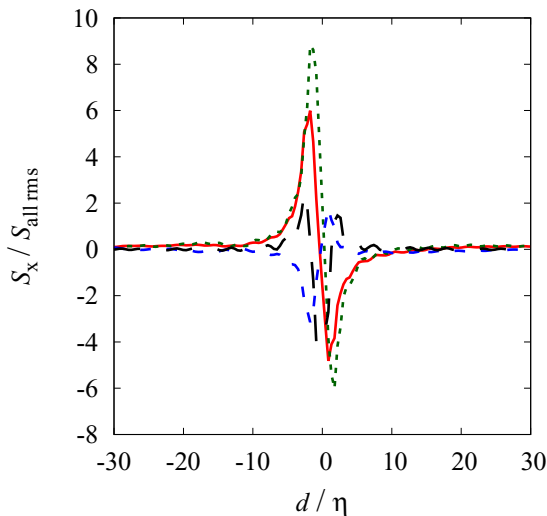


FIG. 21. Sound source distributions in Lilley’s decomposition across shocklets for $M_{t0} = 1.0$, $R_{\lambda 0} = 130$: — (red), term total S_{all} ; \cdots (green), momentum term S_{mom} ; - - (blue), enthalpy term S_{enth} ; - · - (black), viscous term S_{vis} . The values are normalized by the rms value of the term total, $S_{\text{all rms}}$. The positive and the negative d show the upstream and the downstream of the shocklets, respectively.

characteristics of crackle such as the acoustic wave spectra. Second, the recent papers by Buchta and Freund [19], Pineau and Bogey [20] did not discuss the fine-scale turbulent structure and generated acoustic waves in detail. Thus, the contributions from the fine-scale turbulent structure to the crackle noise generation is still unclear, and the present paper are believed to give a clue for them. Here, a possible explanation is given with the present results to one of the remaining open points of the contribution from the fine-scale turbulence to the generation mechanisms of crackle.

In high-thrust military aircraft jets that are widely known to generate crackle noise, the Mach number becomes $M > 1.5$ accompanying the turbulent Mach number becoming larger $M_t > 0.4$. Then the locally supersonic velocity fluctuations appear to generate shocklets. The generated shocklets themselves become strong sound sources having high wave number components and are propagated to the far field, leading to high wave number acoustic waves. An our previous study of the DNS of temporally evolving turbulent shear layer [59] supported the explanation. The study showed that high convective Mach number cases $M_c \geq 1.5$ lead to higher turbulent Mach number $M_t \geq 0.48$ in the most shear layer, which corresponds to $M_{t0} = 1.0$ for the present paper in which shocklets have large contributions on sound sources leading to high wave number components in sound source spectra (see Fig. 7). Our previous study [59] also demonstrated that the near-field pressure spectra for cases $M_c \geq 1.5$ show higher wave number components that do not exist in lower convective Mach number cases $M_c < 1.5$. Those results indicate that the shocklets in high turbulent Mach numbers would create the higher wave number components in the acoustic waves.

The discussion above has shown that the generation of shocklets in high turbulent Mach number flows can affect the propagated acoustic wave characteristics, qualitatively. Toward a more quantitative discussion, one possible future work would be solving the acoustic waves generated by isotropic turbulence following the previous papers [4,5,7,8], where both linear and nonlinear prediction methods would be considered for the acoustic field computation. The study should give us the opportunities for quantitative discussion of the effects of shocklets in high turbulent Mach number flows on the acoustic wave characteristics. In that study, a step-by-step investigation would be suggested. First, far-field acoustic waves generated by decaying isotropic turbulence are

discussed based on the present study. Then the targeted flow is changed to the forced isotropic turbulence to obtain better-averaged statistics.

IV. CONCLUSIONS

In this study, sound source characteristics generated by shocklets in isotropic compressible turbulence are investigated using direct numerical simulations and the source terms of the Lighthill equation with the highest initial turbulent Mach number of $M_{t0} = 1.0$. In order to clarify the difference with the low turbulent Mach number flows, various turbulent Mach numbers $M_{t0} = 0.2-1.0$ have been analyzed. The results show that two sound generation mechanisms appear depending on the turbulent Mach numbers affecting the presence of shocklets.

In the low turbulent Mach number flows, the sound source terms are generated by vortical motion; thus, the Reynolds stress term is one of the main sound sources, as expected. On the other hand, the entropy term cannot be negligible even in the low turbulent Mach numbers. The spectra show that the contribution is mainly given by high wave number components, because it is generated by the viscous effects in the limited Reynolds number we computed. In addition, since the entropy term is generated by the viscous effects caused by velocity difference or vortical motion, the Reynolds stress term (caused by vortical motion), and the entropy term show a positive correlation. From the given results, we indicate that there is a case that the Reynolds number is high enough for the viscous term S_{vis} to be negligible, but not high enough for neglecting the entropy term S_{en} . For the Reynolds number dependence, the larger peak values and smaller-scale structures in sound sources appear with increasing Reynolds numbers due to more active turbulent motion.

In contrast, in the high turbulent Mach numbers, eddy shocklets become important sound sources in addition to sources caused by vortical motion. All source terms show strong values across or on the shocklets. The Reynolds stress and entropy terms have opposite signs near and across the shocklets. The opposite signs between those terms are explained analytically using a one-dimensional shock relation. Similarly, the distribution of the viscous term across shocklets is explained as well. The high turbulent Mach number and the Reynolds number lead to stronger shocklets and subsequently stronger sound sources.

The different sound generation mechanism between low and high turbulent Mach numbers leads to different characteristics of the sound sources. The strength of each source term normalized by the strength of the overall sound sources considerably changes depending on the turbulent Mach number. For $M_{t0} = 0.2$, the normalized sound source strength of the Reynolds stress term and the entropy term are approximately 0.5 and 0.25. Further, the normalized strength of the viscous term is negligible. On the other hand, for $M_{t0} = 1.0$, the values of the Reynolds stress, entropy, and viscous terms change to 1.2, 0.4, and 0.1, respectively. Each component of the sound sources also demonstrate the velocity dependence on sound source strength and increase of their velocity exponents with increasing the turbulent Mach number. For the low turbulent Mach numbers ($M_{t0} \leq 0.4$), the exponent of the Reynolds stress, entropy, and viscous terms are 3.78, 3.75, and 7.81, respectively. For the high turbulent Mach numbers ($M_{t0} \geq 0.9$), the exponent of those same terms increases to 7.41, 5.88, and 15.9, respectively. However, the exponent of the overall sound source strength does not change considerably from the value of ~ 4 because the Reynolds stress term and entropy term cancel each other out in high turbulent Mach numbers due to the existence of shocklets.

Finally, the impact of the generated shocklets on the propagated acoustic wave characteristics is qualitatively discussed. The source terms based on Lilley's decomposition show that the sound sources generated by shocklets have quadruple characteristics at least in unheated high turbulent Mach number flows. Also, it is shown that the generated sound sources by shocklets in high turbulent Mach number flows can affect at least near-field acoustic wave characteristics with high wave number components in the spectra, which would be an explanation for the mechanisms of crackle. In addition, we show that the given results can be used for the improvement of a sound source modeling in a nonlinear acoustic analogy. Toward a more quantitative discussion on the link

between shocklet-generated sound source and acoustic wave characteristics, the study of far-field acoustic wave characteristics is proposed with isotropic turbulence as a future work.

ACKNOWLEDGMENTS

The computations were performed on JAXA Supercomputer System Generation 2 (JSS2) and K computer. This study was supported by JSPS KAKENHI (Grant No. JP15J10408) and partially supported by JSPS KAKENHI (Grants No. 25709009 and No. 17H03473).

APPENDIX: EXTRACTION OF SHOCKLETS

The procedure to extract shocklets and its validity are described here. The shocklets are extracted similarly to previous studies [23,26,37], and it is conducted in the following steps:

- (1) The local minimum of dilatation at $\theta/\theta_{\text{rms}} \leq -3$ is detected.
- (2) The shock normal direction is determined by $\nabla p/|\nabla p|$.
- (3) The physical values (including pressure and density) in the lines of shock normal direction are calculated using trilinear interpolation.
- (4) If the pressure ratio, p_r , and the density ratio, ρ_r , between the upstream and the downstream show $(p_r - 1)(\rho_r - 1) < 0$, the extracted shocklets are not used.
- (5) If the pressure ratio is $p_r < 1$, the pressure ratio is inverted to $1/p_r$ and the density ratio to $1/\rho_r$.
- (6) The reference values of the pressure ratio, p_r , and the density ratio, ρ_r , are determined by a minimum of the following function based on the ideal Rankine-Hugoniot condition:

$$C = \left| \rho_r - \frac{(\gamma + 1)p_r + \gamma - 1}{(\gamma - 1)p_r + \gamma + 1} \right|, \quad (\text{A1})$$

where $C = 0$ corresponds to the values satisfying the Rankine-Hugoniot condition exactly.

Figure 22 depicts the distributions of the dilatation across shocklets for $M_{t0} = 1.0$, $R_{\lambda} = 130$, where d is the distance from the shock and η is the Kolmogorov length scale. The positive and negative d show the upstream and the downstream of the shocklets, respectively. The shape of

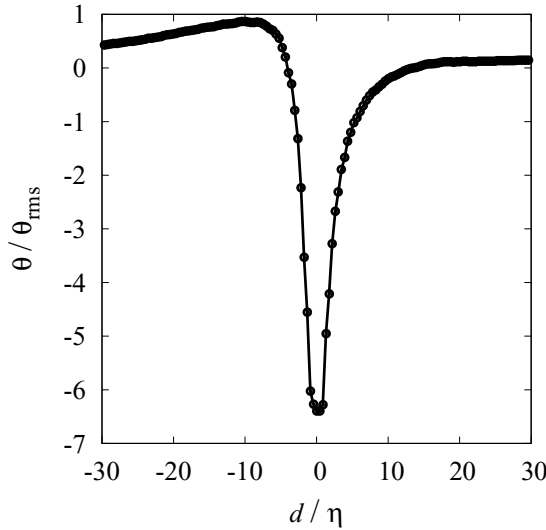


FIG. 22. Distribution of normalized dilatation, $\theta/\theta_{\text{rms}}$, across shocklets for $M_{t0} = 1.0$, $R_{\lambda,0} = 130$. Distance, d , is normalized by the Kolmogorov length scale, η . The positive and the negative d show the upstream and the downstream of the shocklets, respectively.

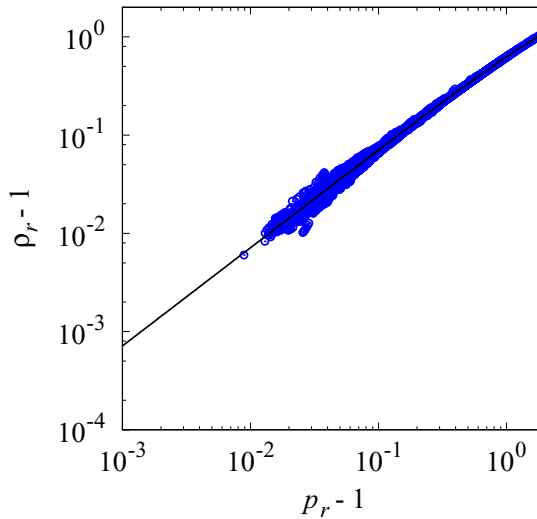


FIG. 23. Pressure ratio, p_r , vs density ratio, ρ_r , in the normal direction to the extracted shocklets for $M_{t0} = 1.0$, $R_{\lambda 0} = 130$. Roughly 22 000 points are used for the scattered plots. The solid line represents the ideal Rankine-Hugoniot condition.

dilatation agrees with that of the extracted shocklets in the previous study [26]. The computed reference values of the pressure ratio, p_r , and density ratio, ρ_r , are shown in Fig. 23 as scatter plots. The plots are distributed on the ideal Rankine-Hugoniot condition represented by the solid line.

-
- [1] M. J. Lighthill, On sound generated aerodynamically. I. General theory, *Proc. R. Soc. A* **211**, 564 (1952).
 - [2] I. Proudman, The generation of noise by isotropic turbulence, *Proc. R. Soc. London A* **214**, 119 (1952).
 - [3] G. M. Lilley, The radiated noise from isotropic turbulence, *Theor. Comput. Fluid Dyn.* **6**, 281 (1994).
 - [4] S. Sarkar and M. Y. Hussaini, Computation of the sound generated by isotropic turbulence, ICASE Technical Report No. 93-74, NASA Langley Research Center Hampton, US, 1993.
 - [5] A. Witkowska, D. Juvé, and J. Brasseur, Numerical study of noise from isotropic turbulence, *J. Comput. Acoust.* **5**, 317 (1997).
 - [6] G. M. Lilley, The radiated noise from isotropic turbulence with applications to the theory of jet noise, *J. Sound Vib.* **190**, 463 (1996).
 - [7] C. Seror, P. Sagaut, C. Bailly, and D. Juvé, Subgrid-scale contribution to noise production in decaying isotropic turbulence, *AIAA J.* **38**, 1795 (2000).
 - [8] C. Seror, P. Sagaut, C. Bailly, and D. Juvé, On the radiated noise computed by large-eddy simulation, *Phys. Fluids* **13**, 476 (2001).
 - [9] G.-W. He, M. Wang, and S. K. Lele, On the computation of space-time correlations by large-eddy simulation, *Phys. Fluids* **16**, 3859 (2004).
 - [10] R. Rubinstein and Y. Zhou, The frequency spectrum of sound radiated by isotropic turbulence, *Phys. Lett. A* **267**, 379 (2000).
 - [11] J. Williams, J. Simson, and V. Virchis, “Crackle”: An annoying component of jet noise, *J. Fluid Mech.* **71**, 251 (1975).
 - [12] K. L. Gee, V. W. Sparrow, M. M. James, J. M. Downing, C. M. Hobbs, T. B. Gabrielson, and A. A. Atchley, The role of nonlinear effects in the propagation of noise from high-power jet aircraft, *J. Acoust. Soc. Am.* **123**, 4082 (2008).
 - [13] J. B. Freund, S. K. Lele, and P. Moin, Compressibility effects in a turbulent annular mixing layer. Part 1. Turbulence and growth rate, *J. Fluid Mech.* **421**, 229 (2000).

- [14] N. D. Cacqueray, C. Bogey, and C. Bailly, Investigation of a high-Mach-number overexpanded jet using large-eddy simulation, *AIAA J.* **49**, 2171 (2011).
- [15] N. D. Cacqueray and C. Bogey, Noise of an overexpanded Mach 3.3 jet: Non-linear propagation effects and correlations with flow, *Int. J. Aeroacoust.* **13**, 607 (2014).
- [16] A. T. Anderson and J. B. Freund, Source mechanisms of jet crackle, in *18th AIAA/CEAS Aeroacoustics Conference (33rd AIAA Aeroacoustics Conference)*, AIAA Paper No. 2012-2251 (AIAA, 2012).
- [17] J. W. Nichols, S. K. Lele, and J. T. Spyropoulos, The source of crackle noise in heated supersonic jets, in *19th AIAA/CEAS Aeroacoustics Conference*, AIAA Paper No. 2013-2197 (AIAA, 2013).
- [18] D. A. Buchta and J. B. Freund, The near-field pressure radiated by planar high-speed free-shear-flow turbulence, *J. Fluid Mech.* **832**, 383 (2017).
- [19] D. A. Buchta and J. B. Freund, Intense sound radiation by high-speed flow: Turbulence structure, gas properties, and near-field gas dynamics, *Phys. Rev. Fluids* **4**, 044605 (2019).
- [20] P. Pineau and C. Bogey, Steepened Mach waves near supersonic jets: study of azimuthal structure and generation process using conditional averages, *J. Fluid Mech.* **880**, 594 (2019).
- [21] T. Passot and A. Pouquet, Numerical simulation of compressible homogeneous flows in the turbulent regime, *J. Fluid Mech.* **181**, 441 (1987).
- [22] S. Lee, S. K. Lele, and P. Moin, Eddy shocklets in decaying compressible turbulence, *Phys. Fluids A* **3**, 657 (1991).
- [23] R. Samtaney, D. Pullin, and B. Kosovic, Direct numerical simulation of decaying compressible turbulence and shocklet statistics, *Phys. Fluids* **13**, 1415 (2001).
- [24] S. Pirozzoli and F. Grasso, Direct numerical simulations of isotropic compressible turbulence: Influence of compressibility on dynamics and structures, *Phys. Fluids* **16**, 4386 (2004).
- [25] S. Kida and S. A. Orzag, Enstrophy budget in decaying compressible turbulence, *J. Sci. Comput.* **5**, 1 (1990).
- [26] J. Wang, Y. Shi, L.-P. Wang, Z. Xiao, X. He, and S. Chen, Effect of shocklets on the velocity gradients in highly compressible isotropic turbulence, *Phys. Fluids* **23**, 125103 (2011).
- [27] J. Wang, Y. Shi, L.-P. Wang, Z. Xiao, X. He, and S. Chen, Effect of compressibility on the small-scale structures in isotropic turbulence, *J. Fluid Mech.* **713**, 588 (2012).
- [28] G. Choi, Y. Li, M. Tanahashi, and T. Miyauchi, Sound generation mechanism in turbulent mixing layer, in *Third Symposium on Turbulence and Shear Flow Phenomena*, Vol. 2 (TSFP Digital Online Library, 2003), pp. 729–734.
- [29] S. A. Miller, Toward a nonlinear acoustic analogy: Turbulence as a source of sound and nonlinear propagation, NASA Technical Memorandum, Tech. Rep. No. NASA/TM2015-218706, NASA Langley Research Center Hampton, US, 2015.
- [30] S. Pirozzoli, Stabilized non-dissipative approximations of Euler equations in generalized curvilinear coordinates, *J. Comput. Phys.* **230**, 2997 (2011).
- [31] T. Nonomura, D. Terakado, Y. Abe, and K. Fujii, A technique for freestream preservation of finite-difference WENO on curvilinear grid, *Comput. Fluids* **107**, 242 (2015).
- [32] X. Y. Hu, Q. Wang, and N. A. Adams, An adaptive central-upwind weighted essentially non-oscillatory scheme, *J. Comput. Phys.* **229**, 8952 (2010).
- [33] F. Ducros, V. Ferrand, F. Nicoud, C. Weber, D. Darracq, C. Gacherieu, and T. Poinso, Large-eddy simulation of the shock/turbulence interaction, *J. Comput. Phys.* **152**, 517 (1999).
- [34] S. Ghosh and W. Matthaeus, Low Mach number two-dimensional hydrodynamic turbulence: Energy budgets and density fluctuations in a polytropic fluid, *Phys. Fluids A* **4**, 148 (1992).
- [35] B. Bayly, C. Levermore, and T. Passot, Density variations in weakly compressible flows, *Phys. Fluids A* **4**, 945 (1992).
- [36] X. Cai, E. E. O’Brien, and F. Ladeinde, Thermodynamic behavior in decaying, compressible turbulence with initially dominant temperature fluctuations, *Phys. Fluids* **9**, 1754 (1997).
- [37] D. Terakado and Y. Hattori, Density distribution in two-dimensional weakly compressible turbulence, *Phys. Fluids* **26**, 085105 (2014).
- [38] S. Kida and S. A. Orzag, Energy and spectral dynamics in forced compressible turbulence, *J. Sci. Comput.* **5**, 85 (1990).

- [39] R. M. Petersen and D. Livescu, Forcing for statistically stationary compressible isotropic turbulence, *Phys. Fluids* **22**, 116101 (2010).
- [40] C. Federrath, J. Roman-Duval, R. S. Klessen, W. Schmidt, and M.-M. M. Low, Comparing the statistics of interstellar turbulence in simulations and observations-solenoidal versus compressive turbulence forcing, *Astron. Astrophys.* **512**, A81 (2010).
- [41] K. Lee, S. S. Girimaji, and J. Kerimo, Effect of compressibility on turbulent velocity gradients and small-scale structure, *J. Turbul.* **10**, N9 (2009).
- [42] A. Bhagatwala and S. K. Lele, Interaction of a Taylor blast wave with isotropic turbulence, *Phys. Fluids* **23**, 035103 (2011).
- [43] A. Bhagatwala and S. K. Lele, Interaction of a converging spherical shock wave with isotropic turbulence, *Phys. Fluids* **24**, 085102 (2012).
- [44] T. Ishida, P. A. Davidson, and Y. Kaneda, On the decay of isotropic turbulence, *J. Fluid Mech.* **564**, 455 (2006).
- [45] H. Miura, Excitations of vortex waves in weakly compressible isotropic turbulence, *J. Turbul.* **5**, N10 (2004).
- [46] J. E. F. Williams, The noise from turbulence convected at high speed, *Proc. R. Soc. A* **255**, 469 (1963).
- [47] M. Tanahashi, T. Miyauchi, and J. Ikeda, Identification of coherent fine scale structure in turbulence, in *IUTAM Symposium on Simulation and Identification of Organized Structures in Flows*, edited by J. N. Sørensen, E. J. Hopfinger, and N. Aubry, Vol. 52 (Springer, Dordrecht, 1999), p. 131.
- [48] M. Tanahashi, S. Iwase, and T. Miyauchi, Appearance and alignment with strain rate of coherent fine scale eddies in turbulent mixing layer, *J. Turbul.* **2**, N6 (2001).
- [49] M. Tanahashi, S.-J. Kang, T. Miyamoto, S. Shimokawa, and T. Miyauchi, Scaling law of fine scale eddies in turbulent channel flows up to $Re_\tau = 800$, *Int. J. Heat Fluid Flow* **25**, 331 (2004).
- [50] M. E. Goldstein, *Aeroacoustics* (McGraw-Hill, New York, 1976).
- [51] N. S. Vaghefi and C. K. Madnia, Local flow topology and velocity gradient invariants in compressible turbulent mixing layer, *J. Fluid Mech.* **774**, 67 (2015).
- [52] J. Panda, R. G. Seasholtz, and K. A. Elam, Investigation of noise sources in high-speed jets via correlation measurements, *J. Fluid Mech.* **537**, 349 (2005).
- [53] C. Bogey and C. Bailly, An analysis of the correlations between the turbulent flow and the sound pressure fields of subsonic jets, *J. Fluid Mech.* **583**, 71 (2007).
- [54] O. M. Phillips, On the generation of sound by supersonic turbulent shear layers, *J. Fluid Mech.* **9**, 1 (1960).
- [55] G. M. Lilley, On the noise from jets, Tech. Rep. No. CP-131, AGARD (1974).
- [56] T. Colonius, S. K. Lele, and P. Moin, Sound generation in a mixing layer, *J. Fluid Mech.* **330**, 375 (1997).
- [57] G. M. Lilley, Jet noise classical theory and experiments, in *aeroacoustics of flight vehicles theory and practice*, Tech. Rep. No. NASA-RP-1258, Chap. 4, NASA Langley Research Center Hampton, US, 1991.
- [58] D. J. Bodony and S. K. Lele, Low-frequency sound sources in high-speed turbulent jets, *J. Fluid Mech.* **617**, 231 (2008).
- [59] D. Terakado, T. Nonomura, A. Oyama, and K. Fujii, Mach number dependence on sound sources in high Mach number turbulent mixing layer, in *22nd AIAA/CEAS Aeroacoustics Conference*, AIAA Paper No. 2016-3015 (AIAA, 2016).

Correction: Byline footnotes for the third and sixth authors were erroneously added during the production cycle and have been removed. Two minor wording errors in text have been fixed. A reference citation was removed from the last paragraph of the Conclusions section.